Tidal behavior of a well in a relatively thick semiconfined aquifer

Xunfeng Lu[1], Kozo Sato[1,2*], and Roland N. Horne[1*]

[1]Department of Energy Science and Engineering, Stanford University, Stanford, CA, USA,
[2]Graduate School of Engineering, The University of Tokyo, Tokyo, Japan
[*]Corresponding author: Roland N. Horne (horne@stanford.edu); Kozo Sato (sato@frcer.t.u-tokyo.ac.jp)

Key Points:

- Solutions for tidal responses were derived for both vertical and horizontal wells situated in a relatively thick semiconfined aquifer.
- A nondimensional number was derived mathematically, forming the basis for the criterion to assess the validity of the existing solutions.
- The new solution was applied to the case of the Arbuckle aquifer to demonstrate the improved validity of the new solution.

Abstract

Subsurface tidal analysis requires only continuous pressure monitoring data and therefore can be a cost-effective technique for estimating aquifer properties. The tidal behavior of a well in a semiconfined aquifer can be described by a diffusion equation that includes a leakage term. This approach is valid for thin aquifers, as long as the overlying layer has low permeability relative to the main aquifer. However, in cases where the aquifer is not thin and the permeability of the overlying layer is not low, using the existing solutions based on these approximations may lead to unsatisfactory outcomes. Alternative solutions for both vertical and horizontal wells were obtained by solving the standard diffusion equation, with leakage expressed as a boundary condition. Furthermore, a nondimensional number was derived mathematically, which forms the basis for a quantitative criterion to assess the applicability of the existing solutions. In the case of a vertical well, the existing solution exhibits acceptable error only if the nondimensional number is less than 0.245. Our new solution extends this upper limitation to 0.475. However, when the number is greater than 0.475, both the existing solution and our new solution are invalid due to the invalid uniform flowrate assumption. For a horizontal well, when the number is less than 0.245, the existing solution is suitable with acceptable error. Our new solution effectively overcomes this limitation. Finally, the new solution was applied to the case of the Arbuckle aquifer to demonstrate the improved validity of the new solution compared to the existing one.

1. Introduction

1.1 Earth tides and its application

Earth tides are the deformation of the solid Earth’s surface caused by the gravitational attraction of the Moon and the Sun. The gravitational pull of these celestial bodies causes a tidal force on the Earth, which results in the deformation of the Earth's surface, primarily in the form of vertical displacement. The magnitude and phase of the Earth tides vary according to the positions of the Moon and the Sun in relation to the Earth (Melchior, 1966). Earth tides can be calculated by theoretical Earth model given the location and time (Matsumoto, et al., 2001; Agnew, 2012).

Earth tides are naturally occurring and offer an opportunity to infer subsurface information. The downhole pressure in closed wells or water level in open wells may include periodic signals with dominantly diurnal and semidiurnal periods induced by Earth tides. Analyzing these oscillatory signals enables the evaluation of various aquifer properties, such as permeability, wellbore storage, skin effect, and CO_2 saturation, by calculating the phase difference and amplitude ratio between the recorded pressure/water level fluctuations and the corresponding theoretical tides (Bredehoeft, 1967; Robinson & Bell, 1971; Gieske & De Vries, 1985; Merritt, 2004; Doan et al., 2006; Cutillo & Bredehoeft, 2011; McMillan et al., 2019; Simon et al., 2021; Liang et al., 2022).

1.2 Tidal response models of confined and semiconfined aquifers to Earth tides

The study of how confined aquifers respond to Earth tides has a rich history and yields valuable information about aquifers. Key analysis parameters include amplitude ratio and phase difference. Amplitude ratio, the ratio between response tidal signals and theoretical tides, can provide insight into the poroelastic properties of the aquifer, including Skempton’s coefficient, pore compressibility, and CO_2 saturation. Analyzing the amplitude ratio has been explored in previous studies by Jacob (1939), Arditty et al. (1978), Van der Kamp & Gale (1983), Rojstaczer & Agnew (1989), Wang (1993), Dean et al. (1994), Sato (2006), Burbey (2010), Burbey et al. (2012), Sato & Horne (2018), and Sato et al. (2022). On the other hand, the phase difference between tidal responses and theoretical tides is more closely related to the flow properties of the aquifer, such as permeability, transmissivity, and skin effect, as seen in previous studies like Hsieh et al. (1987), Xue et al. (2013), Lai et al. (2014), Wang et al. (2018), Gao et al. (2020), Zhu & Wang (2020), Zhang et al. (2021), and Lu et al. (2022).

While extensive research has been conducted on the tidal behavior of confined aquifers, studies of tidal behavior within semiconfined aquifers have been fewer. In a semiconfined aquifer, flow occurs both from the aquifer to wells and at the interface between the aquifer and the permeable layer above it, known as an aquitard. Recognizing that many aquifers may not be perfectly confined, the consideration of leakage is essential in these semiconfined systems. Such consideration contributes to the safety monitoring of groundwater resources, the security of underground repositories, and the detection of CO_2 leakage. Allègre et al. (2016) utilized a vertical flow model to infer permeability from tidally induced water level variations, without accounting for horizontal flow. Their findings, compared with conventional large-scale pumping tests, revealed consistent hydraulic properties. Wang et al. (2018) expanded upon Hsieh's model (Hsieh et al., 1987) by introducing the concept of specific leakage to the diffusion equation as a volumetric source term and then presented a model for understanding the tidal response in a vertical well to Earth tides in aquifers with both horizontal flow and vertical leakage. Provided that transmissivity and storativity are determined independently, this model can be employed to estimate aquitard leakage by analyzing the phase shift and amplitude ratio. The authors put this model into practice in a US Geological Survey deep monitoring well located in the Arbuckle aquifer in Oklahoma, with their analysis highlighting significant leakage at the site. Gao et al. (2020) proposed new models based on work by Hsieh et al. (1987) and Wang et al. (2018) for tidal analysis that incorporate skin and wellbore storage effects. These models are designed for application to vertical wells situated in confined aquifers with only horizontal flow or in semiconfined aquifers with both horizontal and vertical flow. Capable of accurately assessing information related to aquifers through tidal analysis, the proposed models were tested and validated using real-world examples in both confined and semiconfined aquifers, thereby showcasing their practical applications. Lu et al. (2022) derived and solved tidal response models for analyzing tidal response in a horizontal well, considering factors such as skin effect and wellbore storage across three traditional types of aquifers: confined, semiconfined, and those with mixed boundaries. The authors conducted a variable condition analysis to investigate how different parameters, including wellbore storage, skin effect, and vertical leakage, impact the tidal behavior.

It is noted that one of the main assumptions made in previous tidal response models of a semiconfined aquifer is that the overlaying layer has significantly lower hydraulic conductivity than the main aquifer (not an unreasonable assumption in nature). Consequently, leakage from the main aquifer is assumed to be uniformly distributed along the thickness of the main aquifer if it is relatively thin (not always a good assumption in nature because many aquifers are not relatively thin). This simplification replaces the actual flow system with a hypothetical one involving an impermeable confined aquifer, and a diffusion equation incorporating the effect of leakage as a volumetric source term is derived to approximate the flow in such leaky systems (Hantush, 1960; Wang et al., 2018; Gao et al., 2020; Lu et al., 2022). However, this model may not be accurate for systems where the main aquifers are not relatively thin and the permeabilities of the overlaying layer are not relatively low, and in those cases, the standard diffusion equation with leakage expressed as a boundary condition should be used for a more precise mathematical analysis. Hantush (1967) derived such a model where the standard diffusion equation was solved with leakage expressed as a boundary condition to analyze the pump test results. Then, a quantitative criterion was established for the applicability of the solutions that were used in the analysis of pump test. However, the study did not take the tidal force into consideration, which means the author did not incorporate tidal stress term in the diffusion equation. Such types of solutions and quantitative analyses remain an unexplored domain within the field of subsurface tidal analysis. Another assumption made in the previous tidal response models is the uniform flow rate along the wellbore. The quantitative criterion to assess the validity of this assumption should also be analyzed.

In this study, new tidal response models of a semiconfined aquifer were derived and solved with leakage expressed as a boundary condition, as it happens naturally in the physical system. Well arrangements (vertical well and horizontal well), skin effect, and wellbore storage are both considered in the new models. Moreover, comparisons with existing solutions were analyzed and a quantitative criterion was established to determine the suitability of the existing solutions derived from the approximate theory that is currently in use and to assess the validity of uniform flow rate assumption quantitatively. Finally, the application of the new model was demonstrated with real-world examples based on previous work by Wang et al. (2018) and Gao et al. (2020).

2. Tidal response model for a vertical well in a semiconfined aquifer

Vertical wells are very common in water resources utilization and oil and gas industries. This section describes the development of a tidal response model for a vertical well in a semiconfined aquifer with skin and wellbore storage considered and with leakage expressed on the boundary condition. A schematic of a vertical well placed in a semiconfined aquifer system is shown in Figure 1. The target aquifer is located beneath a permeable aquitard, and above the permeable aquitard is an unconfined aquifer. r_w is the wellbore radius. h and b' are the thickness of the aquifer and permeable aquitard respectively. r_s is the radius of damaged zone that causes the skin effect and the pressure drop at the wellbore caused by skin effect is Δp_s. The definition of the skin factor is $S = \Delta p_s \big/ (r\frac{\partial p}{\partial r})_{r=r_w}$, where pressure p represents the excess pressure in the aquifer above the initial baseline pressure. The assumptions for this model are as follows: (1) both the aquifer and aquitard are laterally infinite; (2) the permeable aquitard has negligible storage and is incompressible; (3) the aquifer and aquitard are isotropic and homogeneous; (4) flow rate is uniform along the wellbore.

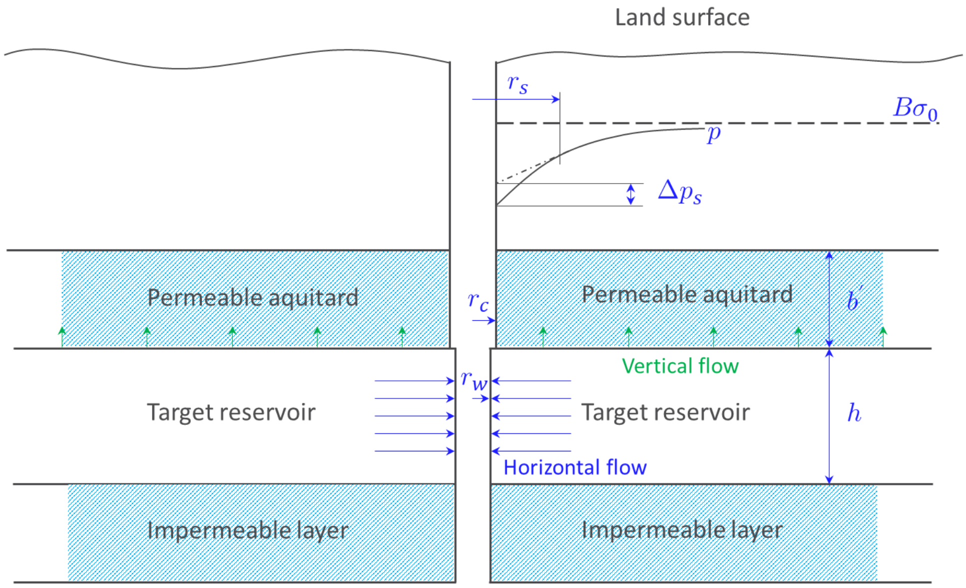

Figure 1: A vertical well placed in a semiconfined aquifer system.

Then the flow transient for a vertical well in a semiconfined aquifer system like Figure 1 under the cubic tidal stress σ_t is governed by:

$$\frac{\partial^2 p}{\partial x^2}+\frac{\partial^2 p}{\partial y^2}+\frac{\partial^2 p}{\partial z^2}=\frac{1}{\eta}\left(\frac{\partial p}{\partial t}-B\frac{\partial \sigma_t}{\partial t}\right),\ \text{here}\ \eta=\frac{k}{\phi\mu C_t} \quad (1.)$$

Here, p equal to $p(m,t)$ is the excess pressure at point m in the aquifer above the initial baseline pressure, so $p(m,t)=p_{absolute}-p_{initial}$. The hydraulic conductivity of the aquifer is $\eta={}^{k}/_{\phi\mu c_t}$ where k, ϕ, μ, and c_t are permeability, porosity, fluid viscosity, and total compressibility respectively. B is the Skempton coefficient, which is defined as the ratio of the change of pore pressure to the change of stress loading under undrained conditions (Skempton, 1954; Wang, 2000).

The initial condition is $p(m,t)|_{t=0}=0$. The outer boundary conditions at $x=\pm\infty$ and $y=\pm\infty$ are

$$p(m,t)|_{x=\pm\infty,y=\pm\infty}=B\sigma_t \quad (2.)$$

The inner boundary at the wellbore is a flow rate boundary. Considering the effect of skin and wellbore storage, inner boundaries are governed by:

$$q(t)=\frac{2\pi kh}{\mu}\left(r\frac{\partial p}{\partial r}\right)_{r=r_w}=C\frac{dp_w}{dt},\quad p_w=\left[p-S\frac{q(t)\mu}{2\pi kh}\right]_{r=r_w} \quad (3.)$$

Here, $q(t)$ is the flow rate from the aquifer into the wellbore, named the sand face flow rate. This boundary condition means that the sand face flow rate is equal to the wellbore flow. C is the wellbore storage caused by fluid expansion or changing liquid level. For a fluid expansion storage coefficient, $C=c_wV_w$, where V_w is the volume of the wellbore, and c_w is the compressibility includes the volume changes in the tubing and casing. For a falling liquid level storage coefficient, $C=\frac{A_w}{\rho g}$, where

A_w is the cross-sectional area of the wellbore in the region where the liquid level is falling (Horne, 1995). S is skin effect and p_w is the pressure measured inside the wellbore.

The boundary condition at $z = 0$ is an impermeable boundary, which is

$$\left.\frac{\partial p}{\partial z}\right|_{z=0} = 0 \tag{4.}$$

The boundary condition at $z = h$ is a permeable boundary, which is a Robin boundary as

$$\left.\frac{k'}{\mu b'} p\right|_{z=h} + \left.\frac{k}{\mu}\frac{\partial p}{\partial z}\right|_{z=h} = 0 \tag{5.}$$

This boundary is the main point of departure from previous research (Hantush, 1960; Wang et al., 2018; Gao et al., 2020; Lu et al., 2022), where researchers modeled the leakage from the aquifer to the permeable aquitard as a volumetric source term in the diffusion equation and then the semiconfined aquifer is simplified as a confined aquifer and the permeable boundary degenerates into an impermeable boundary. The discussion and analysis in this article mainly revolve around the changes to this boundary condition.

2.1 Helper function: solution of a point source

To solve the governing equation (Equation 1) associated with boundary conditions Equation 2 – Equation 5, we can define a helper function, the solution of a point source in the same aquifer system and then integrate the helper function along the z direction from $z = 0$ to $z = h$ to obtain the final solution for the tidal behavior of a vertical well in a semiconfined aquifer. The helper model is shown in Figure 2 (Thambynayagam, 2011). An infinite continuum in the regions $-\infty < x < \infty, -\infty < y < \infty$ and finite in the region $0 < z < h$. Point source at $S_p \equiv (x_0, y_0, z_0)$ at time $t = t_0$ and $-\infty < x_0 < \infty, -\infty < y_0 < \infty, 0 < z_0 < d, t_0 \geq 0$. The initial pressure $p(x, y, z, 0) = 0$. The bottom boundary is a Neumann boundary, and the top boundary is a Robin boundary, which are same as Equation 4 and Equation 5. The outer boundaries at $x = \pm\infty$ and $y = \pm\infty$ are also the same as Equation 2.

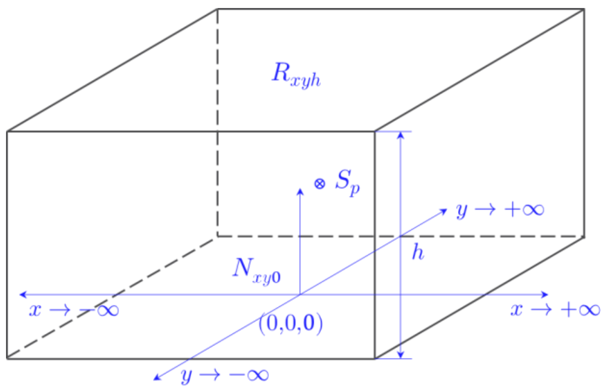

Figure 2: Helper model: pressure transient induced by a point source (from Thambynayagam, 2011).

The assumption is made that the flow rate is uniform along the wellbore, so in the helper model, fluid is produced at the rate of $q_s(t) = q(t)/h$ from $t = t_0$ to $t = t$ at a point (x_0, y_0, z_0). The pressure at point m and time t induced by point source S_p, denoted as $p_s(m, t)$, can be obtained by solving the partial differential equation:

$$\frac{\partial p_s}{\partial t} - B\frac{\partial \sigma_t}{\partial t} = \eta_x \frac{\partial^2 p_s}{\partial x^2} + \eta_y \frac{\partial^2 p_s}{\partial y^2} + \eta_z \frac{\partial^2 p_s}{\partial z^2} + U(t-t_0)\frac{q(t-t_0)}{\phi c_t h}\delta(x-x_0)\delta(y-y_0)\delta(z-z_0) \quad (6.)$$

Associated with initial condition and boundary conditions:

$$\begin{cases} p_s(m,t)|_{t=0} & = 0 \\ p_s(m,t)|_{x=\pm\infty, y=\pm\infty} & = B\sigma_t \\ \left.\frac{\partial p_s}{\partial z}\right|_{z=0} & = 0 \\ \left.\frac{k'}{\mu b'} p_s\right|_{z=h} + \left.\frac{k}{\mu}\frac{\partial p_s}{\partial z}\right|_{z=h} & = 0 \end{cases} \quad (7.)$$

where $U(t-t_0)$ is Heaviside step function and $\delta(x-x_0)$ is delta function.

2.2 Nondimensional form of the helper model and its solution

The nondimensional equations are posed through the following definitions:

$$\begin{matrix} p_{sD} = \dfrac{2\pi k h p_s}{\mu} & B\sigma_D = \dfrac{2\pi k h B\sigma_t}{\mu} & t_D = \dfrac{kt}{\phi\mu c_t (r_w)^2} & C_D = \dfrac{C}{2\pi h \phi c_t (r_w)^2} \\ r_D = \dfrac{r}{r_w} & x_D = \dfrac{x}{r_w} & y_D = \dfrac{y}{r_w} & z_D = \dfrac{z}{r_w} \end{matrix} \quad (8.)$$

If $\eta = \eta_x = \eta_y = \eta_z$ and set $\overline{p_{sD}} = p_{sD} - B\sigma_D$, the nondimensional equation becomes:

$$\frac{\partial \overline{p_{sD}}}{\partial t_D} = \frac{\partial^2 \overline{p_{sD}}}{\partial x_D^2} + \frac{\partial^2 \overline{p_{sD}}}{\partial y_D^2} + \frac{\partial^2 \overline{p_{sD}}}{\partial z_D^2} + 2\pi\frac{q_D(t_D - t_{D0})}{r_w}\delta(x_D - x_{D0})\delta(y_D - y_{D0})\delta(z_D - z_{D0}) \quad (9.)$$

Associated with boundary conditions:

$$\begin{cases} \overline{p_{sD}}|_{t=0} & = 0 \\ \overline{p_{sD}}|_{x=\pm\infty, y=\pm\infty} & = 0 \\ \left.\frac{\partial \overline{p_{sD}}}{\partial z_D}\right|_{z_D=0} & = 0 \\ \left.\frac{\partial \overline{p_{sD}}}{\partial z_D}\right|_{z_D=\frac{h}{r_w}} + \left.\frac{k'}{k b_D}\overline{p_{sD}}\right|_{z_D=\frac{h}{r_w}} & = -\frac{k'}{k b_D} B\sigma_D \end{cases} \quad (10.)$$

The next step is to take the Laplace transform of Equation 9 and Equation 10 for t. The Laplace transformation of function $f(t)$ is $\overline{f(s)} = \int_0^\infty f(t)e^{-st}dt$. Here the Laplace variable is s. We have the following equation:

$$s\overline{p_{sD}} = \frac{\partial^2 \overline{p_{sD}}}{\partial x_D^2} + \frac{\partial^2 \overline{p_{sD}}}{\partial y_D^2} + \frac{\partial^2 \overline{p_{sD}}}{\partial z_D^2} + 2\pi\frac{q_D(s)\exp\left(-st_{D0}\right)}{r_w}\delta(x_D - x_{D0})\delta(y_D - y_{D0})\delta(z_D - z_{D0}) \quad (11.)$$

We then twice take the complex Fourier transformations of Equation 11 and associated boundary conditions for x and y. The complex Fourier transformation of function $f(x)$ is defined by $\overline{f(x)} = \int_{-\infty}^{+\infty} f(x)e^{imx}\,dx$. We have the following equation:

$$s\overline{\overline{\overline{p_{sD}}}} = -m^2\overline{\overline{\overline{p_{sD}}}} - n^2\overline{\overline{\overline{p_{sD}}}} + \frac{\partial^2\overline{\overline{\overline{p_{sD}}}}}{\partial z_D^2} + 2\pi\frac{q_D(s)\exp\,(-st_{D0})}{r_w}\delta(z_D - z_{D0})\exp\,(imx_{D0})\exp\,(iny_{D0}) \quad (12.)$$

Here, m and n are Fourier variables of x and y respectively.

We then take (once) the finite Fourier transformation for z of Equation 12 and associated boundary conditions. For the diffusion system $p(x,t) = f(x)T(t)$ with known and time-dependent Neumann boundary ${\partial p(0,t)}/{\partial x}$ and Robin boundary ${\partial p(h,t)}/{\partial x} + \lambda p(h,t)$, the finite Fourier transformation of function $f(x)$ is:

$$\overline{f(\xi_n)} = \int_0^h f(x)\cos(\xi_n x)dx \quad (13.)$$

and its inversion formula:

$$f(x) = 2\sum_{n=1}^{\infty}\overline{f(\xi_n)}\left\{\frac{\xi_n^2 + \lambda^2}{h(\xi_n^2 + \lambda^2) + \lambda}\right\}\cos(\xi_n x) \quad (14.)$$

Here ξ_n is a positive root of $\xi_n\tan(\xi_n h) = \lambda, n = 1,2, ...$

The finite Fourier cosine transform of the second derivative is obtained by integration by parts:

$$\int_0^h \frac{\partial^2 p(x,t)}{\partial x^2}\cos(\xi_n x)\,dx = -\xi_n^2\bar{p}(\xi_n,t) - \frac{\partial p(0,t)}{\partial x} + \left\{\frac{\partial p(h,t)}{\partial x} + \lambda p(h,t)\right\}\cos(\xi_n h) \quad (15.)$$

After finite Fourier transformation, we have:

$$s\overline{\overline{\overline{\overline{p_{sD}}}}} = -m^2\overline{\overline{\overline{\overline{p_{sD}}}}} - n^2\overline{\overline{\overline{\overline{p_{sD}}}}} - \xi_{nD}^2\frac{\partial^2\overline{\overline{\overline{\overline{p_{sD}}}}}}{\partial z_D^2} + 2\pi\frac{q_D(s)\exp\,(-st_{D0})}{r_w}\cos\,(\xi_{nD}z_{D0})\exp\,(imx_{D0})\exp\,(iny_{D0}) - \frac{k'}{kb_D}\overline{\overline{\overline{\overline{B\sigma_D}}}}\cos\,(\xi_{nD}h_D) \quad (16.)$$

Here, ξ_{nD} is a positive root of $\xi_{nD}\tan(\xi_{nD}h_D) = \lambda_D$, $\lambda_D = {k'}/{kb_D}$.

Simplifying Equation 16:

$$\overline{\overline{\overline{\overline{p_{sD}}}}} = \frac{1}{r_w}\frac{2\pi q_D(s)\exp(-st_{D0})\cos(\xi_{nD}z_{D0})\exp(imx_{D0})\exp(iny_{D0})}{s + m^2 + n^2 + \xi_{nD}^2} + \frac{-\frac{k'}{kb_D}\overline{\overline{\overline{\overline{B\sigma_D}}}}\cos(\xi_{nD}h_D)}{s + m^2 + n^2 + \xi_{nD}^2} \quad (17.)$$

Dividing Equation 17 into two parts p_{sD1}, the first term of p_{sD} that represents the pressure distribution induced by flow at the point source and p_{sD2}, the second term of p_{sD} that represents the pressure distribution induced by the boundary, then taking the inverse Fourier transformation for m and n:

$$\overline{\overline{p_{sD1}}} = \frac{1}{r_w} q_D(s) \exp(-st_{0D}) \cos(\xi_{nD} z_{0D}) K_0\left(\sqrt{((x_{0D} - x_D)^2 + (y_{0D} - y_D)^2)(s + \xi_{nD}^2)}\right) \quad (18.)$$

$$\overline{\overline{p_{sD2}}} = -\lambda_D \overline{B\sigma_D} \cos(\xi_{nD} h_D) \frac{1}{s + \xi_{nD}^2} \quad (19.)$$

Taking the inverse finite Fourier transformation for ξ_{nD} by Equation 14:

$$\overline{p_{sD1}} = \frac{2}{r_w} q_D(s) \exp(-st_{0D}) \sum_{n=1}^{\infty} \cos(\xi_{nD} z_{0D}) \cos(\xi_{nD} z_D) \frac{\xi_{nD}^2 + \lambda_D^2}{h_D(\xi_{nD}^2 + \lambda_D^2) + \lambda_D} K_0\left(\sqrt{((x_{0D} - x_D)^2 + (y_{0D} - y_D)^2)(s + \xi_{nD}^2)}\right) \quad (20.)$$

$$\overline{p_{sD2}} = -2 \sum_{n=1}^{\infty} \lambda_D \overline{B\sigma_D} \cos(\xi_{nD} h_D) \frac{1}{s + \xi_{nD}^2} \frac{\xi_{nD}^2 + \lambda_D^2}{h_D(\xi_{nD}^2 + \lambda_D^2) + \lambda_D} \cos(\xi_{nD} z_D) \quad (21.)$$

2.3 The solution of the vertical well with wellbore storage and skin effect considered

The solution of a vertical well in Laplace space $\overline{p_D}$ can be obtained by firstly, integrating $\overline{p_{sD1}}$ along the wellbore direction from $z_0 = 0$ to $z_0 = h$ to obtain $\overline{p_{D1}}$, and secondly, $\overline{p_{D2}} = \overline{p_{sD2}}$. Then, $\overline{p_D} = \overline{p_{D1}} + \overline{p_{D2}}$. The result of $\overline{p_{D1}}$ is shown here:

$$\begin{aligned} \overline{p_{D1}} = \; & 2q_D(s) \exp(-st_{0D}) \sum_{n=1}^{\infty} \cos(\xi_{nD} z_D) \frac{1}{\xi_{nD}} \sin(\xi_{nD} h_D) \frac{\xi_{nD}^2 + \lambda_D^2}{h_D(\xi_{nD}^2 + \lambda_D^2) + \lambda_D} \\ & K_0\left(\sqrt{((x_{0D} - x_D)^2 + (y_{0D} - y_D)^2)(s + \xi_{nD}^2)}\right) \end{aligned} \quad (22.)$$

Wellbore storage and skin effect can be easily introduced into the final solution via $q_D(s)$ (the details can be found in Lu et al. (2022)) and finally the transfer function between $\overline{p_{wD}}$ (the nondimensional pressure at the wellbore) and the theoretical pressure induced by theoretical Earth tidal stress $\overline{B\sigma_D}$ is:

$$\begin{aligned} H(s) &= \frac{\bar{B} + 1}{1 + C_D S s + C_D s^2 A} \\ \bar{B} &= -2 \sum_{n=1}^{\infty} \frac{(\xi_{nD}^2 + \lambda_D^2)}{h_D(\xi_{nD}^2 + \lambda_D^2) + \lambda_D} \frac{\lambda_D}{s + \xi_{nD}^2} \cos(\xi_{nD} z_D) \cos(\xi_{nD} h_D) \\ A &= \frac{2}{s} \sum_{n=1}^{\infty} \frac{(\xi_{nD}^2 + \lambda_D^2)}{h_D(\xi_{nD}^2 + \lambda_D^2) + \lambda_D} K_0\left(\sqrt{((x_{0D} - x_D)^2 + (y_{0D} - y_D)^2)(s + \xi_{nD}^2)}\right) \cos(\xi_{nD} z_D) \frac{1}{\xi_{nD}} \sin(\xi_{nD} h_D) \end{aligned} \quad (23.)$$

3. Tidal response model for a horizontal well in a semiconfined aquifer

Horizontal wells have been used in many applications, including oil and gas production, geothermal extraction, hazardous waste remediation, and CO_2 sequestration. In this section, a tidal response model for a horizontal well in a semiconfined aquifer is developed with skin and wellbore storage considered and with leakage expressed on the boundary condition. A schematic of a horizontal well living in a semiconfined aquifer system is shown in Figure 3. Notations are the same as in Section 2 for a vertical well, in addition to L representing the length of a horizontal well. The same assumptions are made as follows: (1) both the aquifer and aquitard are laterally infinite; (2) the permeable aquitard has negligible storage and is incompressible; (3) the aquifer and aquitard are isotropic and homogeneous; (4) flow rate is uniform along the wellbore.

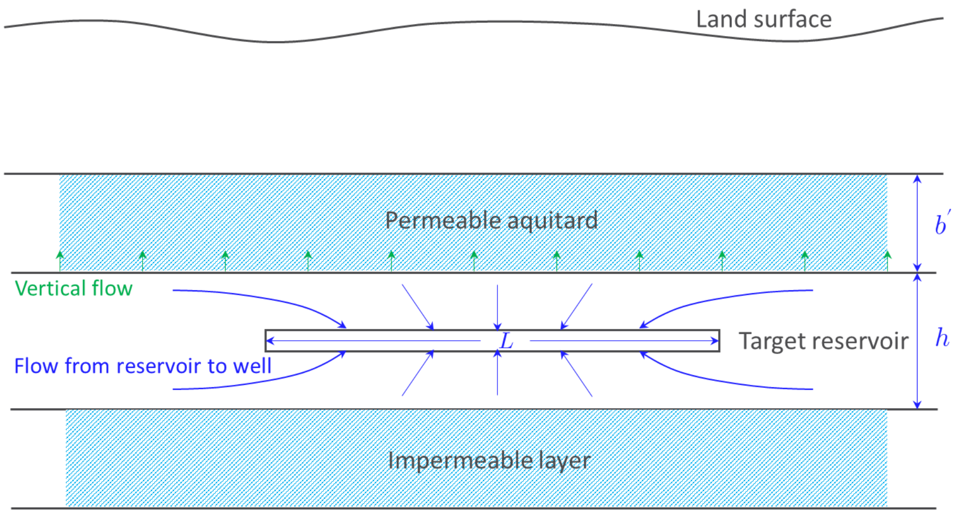

Figure 3: A horizontal well living in a semiconfined aquifer system.

Then the flow transient for a horizontal well in a semiconfined aquifer system like Figure 3 under the cubic tidal stress σ_t is governed by the same governing equation and the same boundary conditions posed previously for a vertical well in a semiconfined aquifer system:

$$\frac{\partial^2 p}{\partial x^2}+\frac{\partial^2 p}{\partial y^2}+\frac{\partial^2 p}{\partial z^2}=\frac{1}{\eta}\left(\frac{\partial p}{\partial t}-B\frac{\partial \sigma_t}{\partial t}\right),\ \text{here}\ \eta=\frac{k}{\phi\mu C_t} \tag{24.}$$

$$\begin{cases} p(m,t)|_{t=0} & =0 \\ p(m,t)|_{x=\pm\infty,y=\pm\infty} & =B\sigma_t \\ \left.\dfrac{\partial p}{\partial z}\right|_{z=0} & =0 \\ \left.\dfrac{k'}{\mu b'}p\right|_{z=h}+\left.\dfrac{k}{\mu}\dfrac{\partial p}{\partial z}\right|_{z=h} & =0 \\ p_w & =\left[p-S\dfrac{q(t)}{2\pi kh}\right]_{r=r_w} \\ q(t) & =\dfrac{2\pi kh}{\mu}\left(r\dfrac{\partial p}{\partial r}\right)=C\dfrac{dp_w}{dt} \end{cases}$$

It is noted that leakage is expressed as a boundary condition instead of expressed as a volumetric source term in the diffusion equation as in earlier research.

3.1 Helper function: solution of a point source

To solve the governing equation associated with boundary conditions Equation 24, we use the same helper model as shown in Figure 2 (described in Section 2) and solve a similar helper function, the solution of a point source in the same aquifer system and then integrate the helper function along the x direction from $x=-L/2$ to $x=L/2$ to obtain the final solution for the tidal behavior of a horizontal well in a semiconfined aquifer. Fluid is produced at the rate of $q_s(t)=q(t)/L$ from $t=t_0$ to $t=t$ at a point (x_0,y_0,z_0). We solve $p_s(m,t)$, the pressure at point m and time t induced by a point source S_p, from the partial differential equation:

$$\frac{\partial p_s}{\partial t} - B\frac{\partial \sigma_t}{\partial t} = \eta_x \frac{\partial^2 p_s}{\partial x^2} + \eta_y \frac{\partial^2 p_s}{\partial y^2} + \eta_z \frac{\partial^2 p_s}{\partial z^2} + U(t-t_0)\frac{q(t-t_0)}{\phi c_t L}\delta(x-x_0)\delta(y-y_0)\delta(z-z_0) \tag{25.}$$

Associated with initial condition and boundary conditions:

$$\begin{cases} p_s(m,t)|_{t=0} & = 0 \\ p_s(m,t)|_{x=\pm\infty, y=\pm\infty} & = B\sigma_t \\ \left.\dfrac{\partial p_s}{\partial z}\right|_{z=0} & = 0 \\ \left.\dfrac{k'}{\mu b'} p_s\right|_{z=h} + \left.\dfrac{k}{\mu}\dfrac{\partial p_s}{\partial z}\right|_{z=h} & = 0 \end{cases} \tag{26.}$$

where $U(t-t_0)$ is Heaviside step function and $\delta(x-x_0)$ is delta function. It is noted that the slight difference between helper function for a vertical well Equation 6 and helper function for a horizontal well Equation 25 is in the definition of $q_s(t)$. The former one is $q_s(t) = q(t)/h$ and the latter one is $q_s(t) = q(t)/L$.

3.2 Nondimensional form of the helper model and its solution

The nondimensional equations are posed through the following definitions:

$$\begin{array}{llll} p_{sD} = \dfrac{2\pi k L p_s}{\mu} & B\sigma_D = \dfrac{2\pi k L B\sigma_t}{\mu} & t_D = \dfrac{kt}{\phi\mu c_t (L/2)^2} & C_D = \dfrac{C}{2\pi L\phi c_t (L/2)^2} \\ r_D = \dfrac{r}{L/2} & x_D = \dfrac{x}{L/2} & y_D = \dfrac{y}{L/2} & z_D = \dfrac{z}{L/2} \end{array} \tag{27.}$$

If $\eta = \eta_x = \eta_y = \eta_z$ and set $\overline{p_{sD}} = p_{sD} - B\sigma_D$, the nondimensional equation becomes:

$$\frac{\partial \overline{p_{sD}}}{\partial t_D} = \frac{\partial^2 \overline{p_{sD}}}{\partial x_D^2} + \frac{\partial^2 \overline{p_{sD}}}{\partial y_D^2} + \frac{\partial^2 \overline{p_{sD}}}{\partial z_D^2} + 4\pi \frac{q_D(t_D - t_{D0})}{L}\delta(x_D - x_{D0})\delta(y_D - y_{D0})\delta(z_D - z_{D0}) \tag{28.}$$

Associated with boundary conditions:

$$\begin{cases} \overline{p_{sD}}|_{t=0} & = 0 \\ \overline{p_{sD}}|_{x=\pm\infty, y=\pm\infty} & = 0 \\ \left.\dfrac{\partial \overline{p_{sD}}}{\partial z_D}\right|_{z_D=0} & = 0 \\ \left.\dfrac{\partial \overline{p_{sD}}}{\partial z_D}\right|_{z_D=\frac{2h}{L}} + \left.\dfrac{k'}{k b_D}\overline{p_{sD}}\right|_{z_D=\frac{2h}{L}} & = -\dfrac{k'}{k b_D} B\sigma_D \end{cases} \tag{29.}$$

After Laplace transformation of Equation 28 and Equation 29 for t, twice complex Fourier transformations for x and y, and once finite Fourier transformation for z, we have:

$$s\overline{\overline{\overline{\overline{\overline{p_{sD}}}}}} = -m^2\overline{\overline{\overline{\overline{\overline{p_{sD}}}}}} - n^2\overline{\overline{\overline{\overline{\overline{p_{sD}}}}}} - \xi_{nD}^2 \frac{\partial^2 \overline{\overline{\overline{\overline{\overline{p_{sD}}}}}}}{\partial z_D^2} + 4\pi \frac{q_D(s)\exp(-s t_{D0})}{L}\cos(\xi_{nD} z_{D0})\exp(i m x_{D0})\exp(i n y_{D0}) - \frac{k'}{k b_D}\overline{\overline{\overline{\overline{B\sigma_D}}}}\cos(\xi_{nD} h_D) \tag{30.}$$

Here, ξ_{nD} is a positive root of $\xi_{nD}\tan(\xi_{nD} h_D) = \lambda_D$, $\lambda_D = {k'}/{k b_D}$.

Simplifying Equation 30:

$$\overline{\overline{\overline{p_{sD}}}} = \frac{1}{L}\frac{4\pi q_D(s)\exp(-st_{D0})\cos(\xi_{nD}z_{D0})\exp(imx_{D0})\exp(iny_{D0})}{s+m^2+n^2+\xi_{nD}^2} + \frac{-\frac{k'}{kb_D}\overline{\overline{\overline{B\sigma_D}}}\cos(\xi_{nD}h_D)}{s+m^2+n^2+\xi_{nD}^2} \quad (31.)$$

Similarly, dividing Equation 31 into two parts p_{sD1}, the first term of p_{sD} that represents the pressure distribution induced by flow at the point source and p_{sD2}, the second term of p_{sD} that represents the pressure distribution induced by the boundary, then taking the inverse Fourier transformation for m and n and inverse finite Fourier transformation for ξ_{nD}:

$$\overline{p_{sD1}} = \frac{4}{L}q_D(s)\exp(-st_{0D})\sum_{n=1}^{\infty}\cos(\xi_{nD}z_{0D})\cos(\xi_{nD}z_D)\frac{\xi_{nD}^2+\lambda_D^2}{h_D(\xi_{nD}^2+\lambda_D^2)+\lambda_D}K_0\left(\sqrt{((x_{0D}-x_D)^2+(y_{0D}-y_D)^2)(s+\xi_{nD}^2)}\right) \quad (32.)$$

$$\overline{p_{sD2}} = -2\sum_{n=1}^{\infty}\lambda_D\overline{B\sigma_D}\cos(\xi_{nD}h_D)\frac{1}{s+\xi_{nD}^2}\frac{\xi_{nD}^2+\lambda_D^2}{h_D(\xi_{nD}^2+\lambda_D^2)+\lambda_D}\cos(\xi_{nD}z_D) \quad (33.)$$

3.3 The solution of the horizontal well with wellbore storage and skin effect considered

The solution of a horizontal well in Laplace space $\overline{p_D}$ can be obtained by firstly setting $x = y = 0$ and integrate $\overline{p_{sD1}}$ along the wellbore direction from $x_0 = -L/2$ to $x_0 = L/2$ to obtain $\overline{p_{D1}}$. Secondly, $\overline{p_{D2}} = \overline{p_{sD2}}$. Then, $\overline{p_D} = \overline{p_{D1}} + \overline{p_{D2}}$. The result of $\overline{p_{D1}}$ is shown here:

$$\overline{p_{D1}} = 4q_D(s)\exp(-st_{0D})\sum_{n=1}^{\infty}\cos(\xi_{nD}z_{0D})\cos(\xi_{nD}z_D)\frac{\xi_{nD}^2+\lambda_D^2}{h_D(\xi_{nD}^2+\lambda_D^2)+\lambda_D}\operatorname{arcsinh}\left(\frac{\pi}{2\sqrt{s+\xi_{nD}^2}}\right) \quad (34.)$$

Similarly, wellbore storage and skin effect can be easily introduced into the final solution via $q_D(s)$ (the details can be found in Lu et al. (2022)) and finally the transfer function between $\overline{p_{wD}}$ (the nondimensional pressure at the wellbore) and the theoretical pressure induced by theoretical Earth tidal stress $\overline{B\sigma_D}$ for a horizontal well is:

$$\begin{aligned} H(s) &= \frac{\bar{B}+1}{1+C_DSs+C_Ds^2A} \\ \bar{B} &= -2\sum_{n=1}^{\infty}\frac{(\xi_{nD}^2+\lambda_D^2)}{h_D(\xi_{nD}^2+\lambda_D^2)+\lambda_D}\frac{\lambda_D}{s+\xi_{nD}^2}\cos(\xi_{nD}z_D)\cos(\xi_{nD}h_D) \\ A &= \frac{4}{s}\sum_{n=1}^{\infty}\frac{(\xi_{nD}^2+\lambda_D^2)}{h_D(\xi_{nD}^2+\lambda_D^2)+\lambda_D}\sinh^{-1}\frac{\pi}{2\sqrt{(s+\xi_{nD}^2)}}\cos(\xi_{nD}z_{wD})\cos(\xi_{nD}z_D) \end{aligned} \quad (35.)$$

4. Comparison with the existing solutions and the quantitative criteria

In this section, the solved solutions Equation 23 and Equation 35 are compared with the previously available solutions. Also, the quantitative criteria are derived to assess the applicability of the existing solutions and the new solutions.

4.1 Comparison with the existing solution of a vertical well: Gao's model

The transfer function of Gao's model (Gao et al., 2020) for a vertical well living in a semiconfined aquifer is shown as:

$$H(i\omega)=\left[1+\frac{\alpha_D^2}{2S_D\beta_D}\frac{K_0(\beta_D)}{K_1(\beta_D)}+\pi i\frac{s}{T_D}\right]^{-1}\left(\frac{\alpha_D}{\beta_D}\right)^2 \tag{36.}$$

Here, $\alpha_D=r_w\sqrt{\frac{i\omega\phi\mu c_t}{k}}=\sqrt{\frac{2\pi i S_D}{T_D}}$, $S_D=\frac{\pi\phi c_t h r_w^2}{C}=\frac{1}{2C_D}$, $T_D=\frac{2\pi^2 kh}{C\mu\omega}=\frac{\pi\tau kh}{C\mu}$, $\beta_D=r_w\sqrt{H'+\frac{i\omega\phi\mu c_t}{k}}=\sqrt{H_D+\alpha_D^2}$, $H'=\frac{K'}{b'T}$ and $H_D=r_w^2H'$. K' is the vertical hydraulic conductivity of the overlaying aquitard and T is the transmissivity of the target aquifer. Replace $i\omega$ using Laplace variable s, Equation 36 can be rewritten as:

$$\begin{aligned} H(s) &= \frac{B}{1+C_DSs+C_Ds^2A} \\ B &= \frac{s}{H_D+s} \\ A &= \frac{1}{s\sqrt{(H_D+s)}}\frac{K_0\left(\sqrt{(H_D+s)}\right)}{K_1\left(\sqrt{(H_D+s)}\right)} \end{aligned} \tag{37.}$$

If leakage is expressed on the boundary, the solution for a vertical well has been solved as Equation 23. Equation 23 is placed here again for the convenience of comparison (set $(x_{0D}-x_D)^2+(y_{0D}-y_D)^2=r_D=1$, the position at wellbore):

$$\begin{aligned} H(s) &= \frac{\bar{B}+1}{1+C_DSs+C_Ds^2A} \\ \bar{B} &= -2\sum_{n=1}^{\infty}\frac{(\xi_{nD}^2+\lambda_D^2)}{h_D(\xi_{nD}^2+\lambda_D^2)+\lambda_D}\frac{\lambda_D}{s+\xi_{nD}^2}\cos(\xi_{nD}z_D)\cos(\xi_{nD}h_D) \\ A &= \frac{2}{s}\sum_{n=1}^{\infty}\frac{(\xi_{nD}^2+\lambda_D^2)}{h_D(\xi_{nD}^2+\lambda_D^2)+\lambda_D}K_0\left(\sqrt{(s+\xi_{nD}^2)}\right)\cos(\xi_{nD}z_D)\frac{1}{\xi_{nD}}\sin(\xi_{nD}h_D) \end{aligned} \tag{38.}$$

Here, ξ_{nD} is a positive root of $\xi_{nD}\tan(\xi_{nD}h_D)=\lambda_D$, $\lambda_D={k'}/{kb_D}=H_Dh_D$.

Starting with:

$$h_D\xi_{nD}\tan(\xi_{nD}h_D)=h_D\lambda_D=\left(h_D\sqrt{H_D}\right)^2 \tag{39.}$$

We can derive a quantitative criterion for a vertical well model to assess the applicability of the previous models like Gao's and Wang's models (Gao, et al., 2020; Wang, et al., 2018).

The first positive root ξ_{0D} is firstly discussed here. The Taylor expansion of $\tan x=x+\frac{1}{3}x^3+O(x^5)$, then Equation 39 becomes if $h_D\xi_{0D}$ is represented by x for the convenience of mathematics:

$$x\left(x+\frac{1}{3}x^3+O(x^5)\right)=\left(h_D\sqrt{H_D}\right)^2 \tag{40.}$$

Because $h_D\sqrt{H_D}$ is a small value, x is also small, then:

$$\frac{1}{3}x^4+x^2-\left(h_D\sqrt{H_D}\right)^2=0 \tag{41.}$$

The solution of Equation 41 is:

$$x^2=\frac{-1+\sqrt{1+\frac{4}{3}\left(h_D\sqrt{H_D}\right)^2}}{\frac{2}{3}} \tag{42.}$$

The Taylor expansion of $\sqrt{1+x}=1+\frac{x}{2}-\frac{x^2}{8}+O(x^3)$, then Equation 42 can be rewritten as:

$$x^2=\left(h_D\sqrt{H_D}\right)^2-\frac{1}{3}\left(h_D\sqrt{H_D}\right)^4+O\left(\left(h_D\sqrt{H_D}\right)^6\right) \tag{43.}$$

If a 1% error is acceptable on x, then $\frac{1}{3}\left(h_D\sqrt{H_D}\right)^4$ should be no more than 2% of $\left(h_D\sqrt{H_D}\right)^2$ and $x^2\approx\left(h_D\sqrt{H_D}\right)^2$, which means

$$\xi_{0D}\approx\sqrt{H_D} \tag{44.}$$

and the quantitative criterion is:

$$h_D\sqrt{H_D}<0.245 \tag{45.}$$

For other positive roots ξ_{nD},

$$\xi_{nD}\approx n\pi/h_D, n=1,2,3\ldots \tag{46.}$$

Inserting Equation 44 and Equation 46 to Equation 38, which is the solution of the new model, and ignoring small terms, then:

$$\overline{B}+1\approx\frac{s}{s+H_D} \tag{47.}$$

which is the term B in Equation 37, the solution of the previous Gao's model.

Additionally, the term A in Equation 38 is approximated as:

$$A\approx\frac{K_0\left(\sqrt{s+H_D}\right)}{s} \tag{48.}$$

For small arguments $0 < |x| \ll \sqrt{\alpha + 1}$, we have:

$$K_\alpha(x) \sim \begin{cases} -ln\left(\frac{x}{2}\right) - \gamma & \text{if } \alpha = 0 \\ \frac{\Gamma(\alpha)}{2}\left(\frac{2}{x}\right)^\alpha & \text{if } \alpha > 0 \end{cases} \tag{49.}$$

So, the term A in Equation 37 can also be simplified given $H_D + s$ is small:

$$A \approx \frac{K_0\left(\sqrt{s + H_D}\right)}{s}$$

which is the same as Equation 48, the approximated value of term A in Equation 38.

Hence, it is demonstrated that we could derive the solution of the previous Gao's model (Equation 37) from the solution of the new model (Equation 38) given the quantitative criterion $h_D\sqrt{H_D} < 0.245$.

Figure 3 illustrates a comparison between Gao's model and the new model under three different values of $h_D\sqrt{H_D}$, ranging from 0.1 to 0.548. The relative error is also examined in the figure. The absolute values of physical parameters to generate Figure 4 are shown in Table 1. Different tidal constituents are marked in the figure and periods of these tidal constituents are listed in Table 2. When $h_D\sqrt{H_D} = 0.1$, the amplitude and phase of transfer function H for Gao's model and new model are almost identical. However, there are larger differences of the amplitude and phase of transfer function H between Gao's model and new model when $h_D\sqrt{H_D} = 0.548$. This means the previous model is not suitable for aquifer with relatively larger $h_D\sqrt{H_D}$. With the increasing frequency, the relative error of amplitude of transfer function between the previous model and new model decreases from more than 12% to less than 5% for $h_D\sqrt{H_D} = 0.548$ while the relative error of phase of transfer function increases rapidly from around 0% to more than 20% for $h_D\sqrt{H_D} = 0.548$. Hence, models should be chosen carefully if the phase difference for semidiurnal tidal constituent and diurnal tidal constituent are analyzed to infer aquifer properties, which is a common method in hydrological applications (McMillan, et al., 2019; Rau, et al., 2022; Valois, et al., 2022).

The amplitude ratio and phase difference between water level and tidal force depend on frequencies of tidal force and vertical leakage coefficient H_D. With the increasing frequency of tides, the amplitude ratio increases and phase advance decreases, which means the aquifer tends to be confined aquifer under tidal force with high frequency and tends to be open aquifer under tidal force with low frequency (Wang, 2000). With the decreasing vertical leakage coefficient, the amplitude ratio increases and phase difference decreases, which is reasonable because the aquifer becomes more confined aquifer.

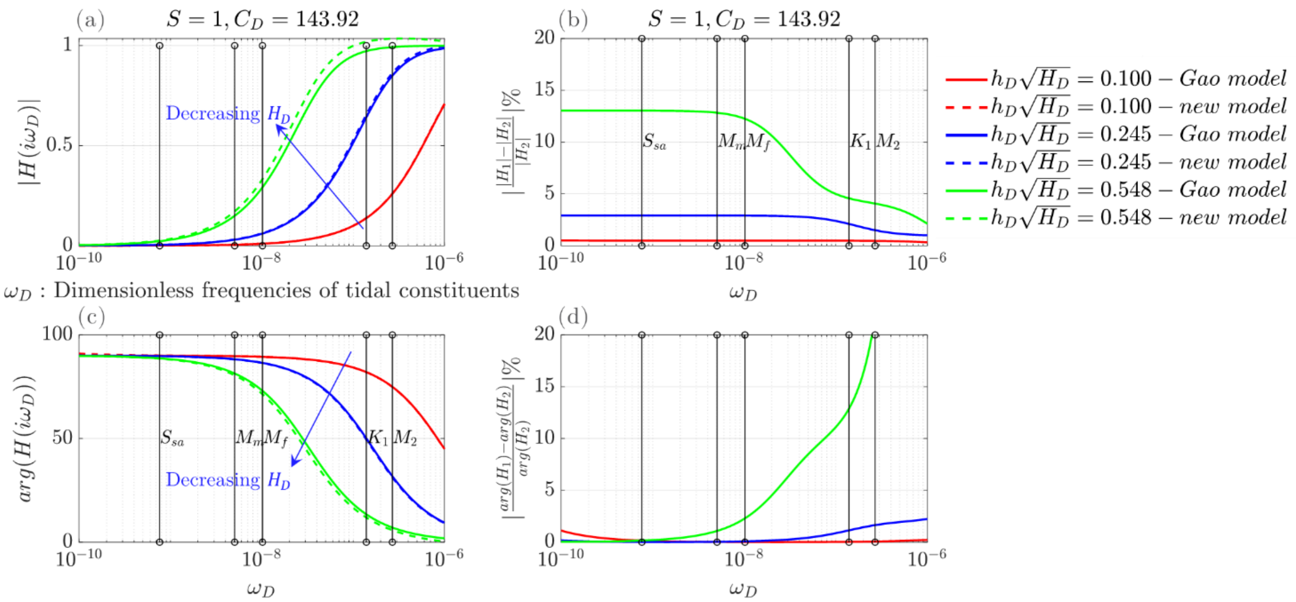

Figure 4: Comparison between Gao's model and the new model under three different values of $h_D\sqrt{H_D}$. (a): the amplitude of the transfer functions; (b): the relative error in amplitude of the transfer functions between Gao's solution and the new solution; (c): the phase of the transfer functions; (d) the relative error in phase of the transfer functions between Gao's solution and the new solution. (S_{sa}: semiannual constituent; M_m: monthly constituent; M_f: Fortnightly constituent; K_1: diurnal constituent; M_2: semidiurnal constituent.)

Table 1: The absolute values of physical parameters to generate Figure 4

Parameters	Values	Parameters	Values
Well radius r_w	0.1 m	Aquifer permeability k	4×10^{-12} m^2
Viscosity μ	0.003 Pa·s	Aquitard permeability	4×10^{-13} m^2
Porosity φ	0.25	Aquitard thickness h	10,60,300 m
Compressibility c_t	1.02×10^{-9} Pa^{-1}	Skin S	1
Aquifer thickness b'	100 m	Wellbore storage C	$2.3059\times10^{-9}\cdot\ h$ m^3

Table 2: Different tidal constituents and its periods

Tidal constituent	Period
M_2	12.421 h
K_1	23.934 h
M_f	13.661 days
M_m	27.555 days
S_{sa}	0.5 yr

4.2 Comparison with the existing solution of a horizontal well: Lu's model

The transfer function of Lu's model (Lu et al., 2022) for a horizontal well living in a semiconfined aquifer is shown as:

$$\begin{aligned} H(s) &= \frac{B}{1 + C_D S s + C_D s^2 A} \\ B &= \frac{s}{s + H_D} \\ A &= \frac{2}{s}\frac{1}{h_D}\sinh^{-1}\frac{\pi}{2\sqrt{s + H_D}} + \frac{4}{s}\sum_{n=1}^{\infty}\frac{1}{h_D}\sinh^{-1}\frac{\pi}{2\sqrt{\left(s + H_D + \left(\frac{n\pi}{h_D}\right)^2\right)}}\cos\frac{n\pi z_{wD}}{h_D}\cos\frac{n\pi z_D}{h_D} \end{aligned} \quad (50.)$$

The solution for a horizontal well if the leakage is expressed in boundary has been solved as Equation 35, which is placed here again for the convenience of comparison:

$$\begin{aligned} H(s) &= \frac{\bar{B} + 1}{1 + C_D S s + C_D s^2 A} \\ \bar{B} &= -2\sum_{n=1}^{\infty}\frac{(\xi_{nD}^2 + \lambda_D^2)}{h_D(\xi_{nD}^2 + \lambda_D^2) + \lambda_D}\frac{\lambda_D}{s + \xi_{nD}^2}\cos(\xi_{nD} z_D)\cos(\xi_{nD} h_D) \\ A &= \frac{4}{s}\sum_{n=1}^{\infty}\frac{(\xi_{nD}^2 + \lambda_D^2)}{h_D(\xi_{nD}^2 + \lambda_D^2) + \lambda_D}\sinh^{-1}\frac{\pi}{2\sqrt{(s + \xi_{nD}^2)}}\cos(\xi_{nD} z_{wD})\cos(\xi_{nD} z_D) \end{aligned} \quad (51.)$$

Here, ξ_{nD} is a positive root of $\xi_{nD}\tan(\xi_{nD} h_D) = \lambda_D$, $\lambda_D = {}^{k'}/_{kb_D} = H_D h_D$.

It should be noted that for horizontal well and vertical well models, although the symbols used are the same, the characteristic length used for nondimensionalization is different. For the horizontal well model, the characteristic length is half well length ($L/2$), but for the vertical well model, the characteristic length is wellbore radius (r_w).

Similarly, starting with $h_D\xi_{nD}\tan(\xi_{nD} h_D) = h_D\lambda_D = \left(h_D\sqrt{H_D}\right)^2$, the quantitative criterion for a horizontal well model can be derived mathematically to assess the applicability of Lu's model (Lu, et al., 2022). The criterion for a horizontal well model is the same with that for a vertical well model: $h_D\sqrt{H_D} < 0.245$, then $\xi_{0D} \approx \sqrt{H_D}$, $\xi_{nD} \approx n\pi/h_D, n = 1,2,3$ ....

Inserting the approximated ξ_{nD} to Equation 51 and ignoring small terms, then:

$$\overline{B} + 1 \approx \frac{s}{s + H_D} \quad (52.)$$

which is the term B of the previous Lu's model Equation 50.

The term A in Equation 51 is approximated as:

$$A \approx \frac{2}{s}\frac{1}{h_D}\sinh^{-1}\frac{\pi}{2\sqrt{s + H_D}} + \frac{4}{s}\sum_{n=1}^{\infty}\frac{1}{h_D}\sinh^{-1}\frac{\pi}{2\sqrt{\left(s + \left(\frac{n\pi}{h_D}\right)^2\right)}}\cos\frac{n\pi z_{wD}}{h_D}\cos\frac{n\pi z_D}{h_D} \quad (53.)$$

Because H_D is small enough compared to $s + \left(\frac{n\pi}{h_D}\right)^2$ given $h_D\sqrt{H_D} < 0.245$, the term A in

Equation 50 could be approximated as:

$$A \approx \frac{2}{s}\frac{1}{h_D}\sinh^{-1}\frac{\pi}{2\sqrt{s+H_D}} + \frac{4}{s}\sum_{n=1}^{\infty}\frac{1}{h_D}\sinh^{-1}\frac{\pi}{2\sqrt{\left(s+\left(\frac{n\pi}{h_D}\right)^2\right)}}\cos\frac{n\pi z_{wD}}{h_D}\cos\frac{n\pi z_D}{h_D} \quad (54.)$$

which is the same as Equation 53, the approximated value of term A in Equation 51.

Similarly, we show that the solution of the previous Lu's model (Equation 50) could be derived from the solution of the new model (Equation 51) given the quantitative criterion $h_D\sqrt{H_D} < 0.245$.

Figure 5 provides a comparison between Lu's model and the new horizontal model under three different values of $h_D\sqrt{H_D}$, ranging from 0.1 to 0.548. Within this range, the relative error is also examined. The absolute values of physical parameters used to generate Figure 5 are laid out in Table 3. The figure also marks different tidal constituents, with the periods of these tidal constituents detailed in Table 2. When $h_D\sqrt{H_D} = 0.1$, there is a close resemblance between the amplitude and phase of the transfer function for both Lu's model and the new model. However, as $h_D\sqrt{H_D}$ increases to 0.548, a noticeable difference between Lu's model and the new model emerges in the amplitude and phase of the transfer function. This discrepancy implies that the previous model becomes unsuitable for aquifers with relatively larger values of $h_D\sqrt{H_D}$. As the frequency increases, the relative error in amplitude of the transfer function between the previous model and the new model decreases from over 10% to less than 2% for $h_D\sqrt{H_D} = 0.548$. Conversely, the relative error in the phase of the transfer function escalates rapidly from approximately 0% to more than 10% for the same value of $h_D\sqrt{H_D}$. Therefore, selecting the appropriate model requires careful consideration, especially when analyzing the phase difference for semidiurnal tidal constituents and diurnal tidal constituents to infer aquifer properties. In addition, the dependence of amplitude ratio and phase difference between water level and tidal force in a horizontal well on frequencies of tidal force and vertical leakage coefficient H_D is similar to that in a vertical well.

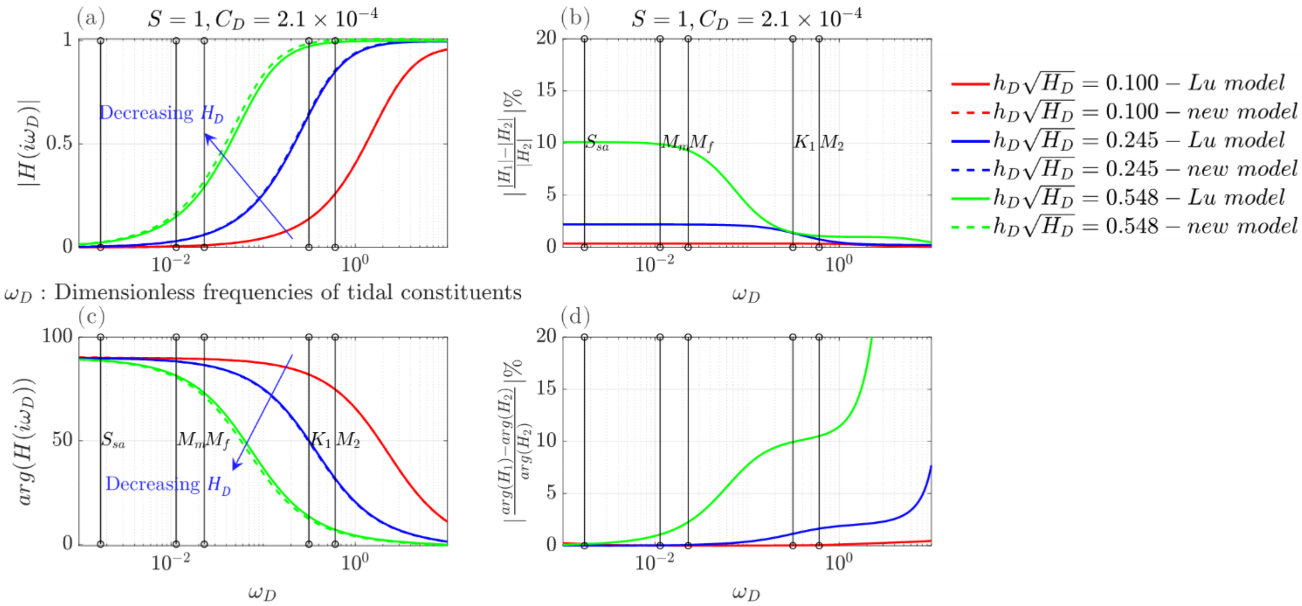

Figure 5: Comparison between Lu's model and the new model under three different values of $h_D\sqrt{H_D}$. (a): the amplitude of the transfer functions; (b): the relative error in amplitude of the transfer functions between Lu's solution and the new solution; (c): the phase of the transfer functions; (d) the relative error in phase of the transfer functions between Lu's solution and the new solution. (S_{sa}: semiannual constituent; M_m: monthly constituent; M_f: Fortnightly constituent; K_1: diurnal constituent; M_2: semidiurnal constituent.)

Table 3: The absolute values of physical parameters to generate Figure 5

Parameters	Values	Parameters	Values
Well radius r_w	0.1 m	Aquifer	4×10^{-12} m^2
Viscosity μ	0.003 Pa·s	Aquitard	4×10^{-13} m^2
Porosity φ	0.25	Aquitard thickness	10,60,300 m
Compressibility c_t	1.02×10^{-9}	Skin S	1
Aquifer thickness b'	100 m	Wellbore storage C	2.3059×10^{-6} m^3 /Pa
Well length l	300 m		

4.3 Relative error variation with skin effect S, frequencies of tidal force, and thickness of aquifer

Figure 6 and Figure 7 illustrate the variation in relative errors between the approximate solutions and the new solutions with the skin effect (S), the frequencies of tidal force, and the nondimensional thickness of aquifer (h_D) for a vertical well and a horizontal well in a semiconfined aquifer respectively. Except for the skin effect and the thickness of aquifer, the values of other parameters align with those listed in Table 1 and Table 3.

These figures clearly demonstrate that the skin effect has negligible impact on the relative errors, while both the thickness of aquifer and the frequencies of tidal force exert significant influence on these errors. More precisely, an increase in aquifer thickness results in higher relative errors in both the amplitude and phase of the transfer function. As for the frequencies of tidal force, a tidal constituent with a high frequency leads to smaller relative errors in the amplitude of the transfer function but larger errors in its phase.

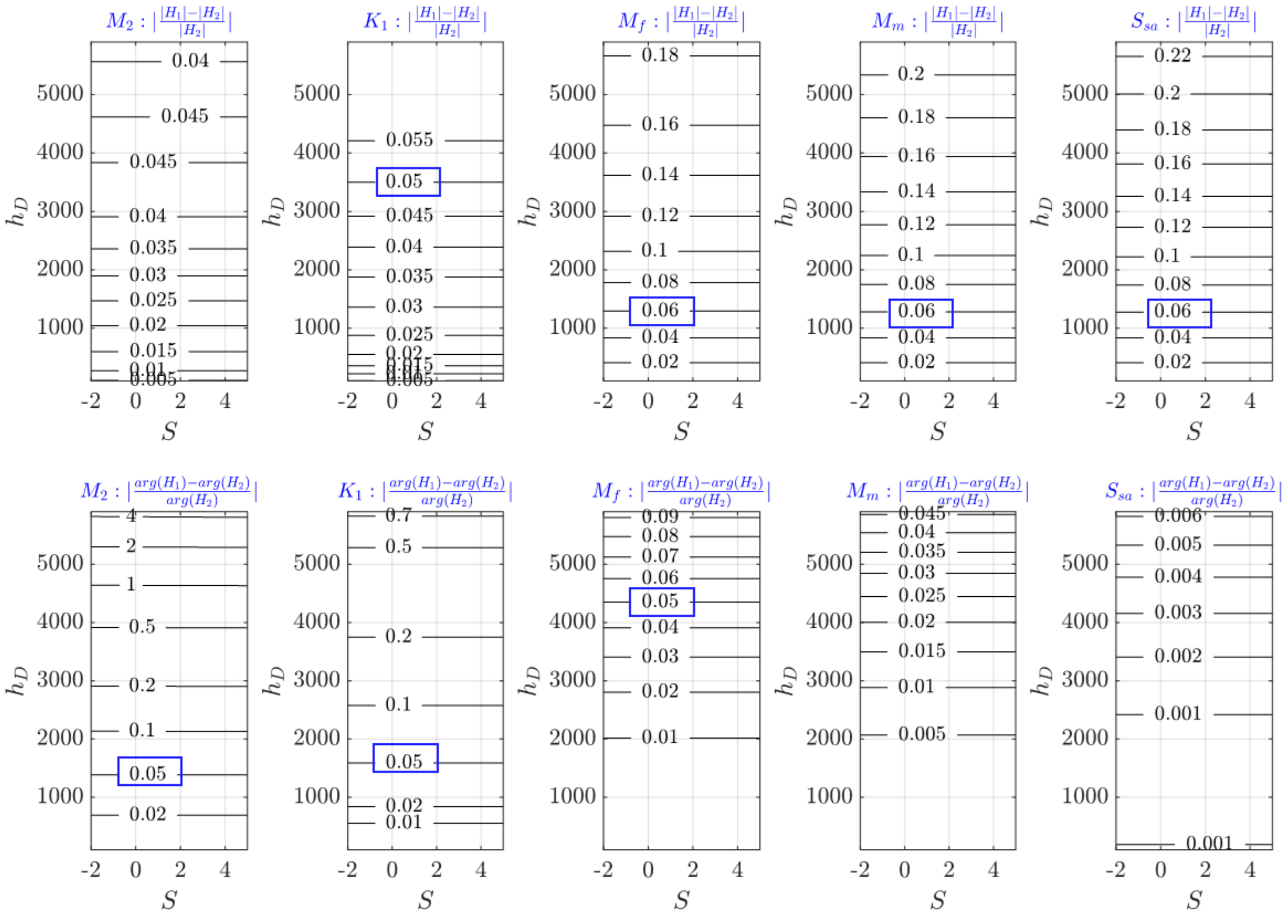

Figure 6: The variation in relative errors between the approximate solutions and the new solutions with the skin effect (S), the frequencies of tidal force, and the nondimensional thickness of aquifer (h_D) for a vertical well.

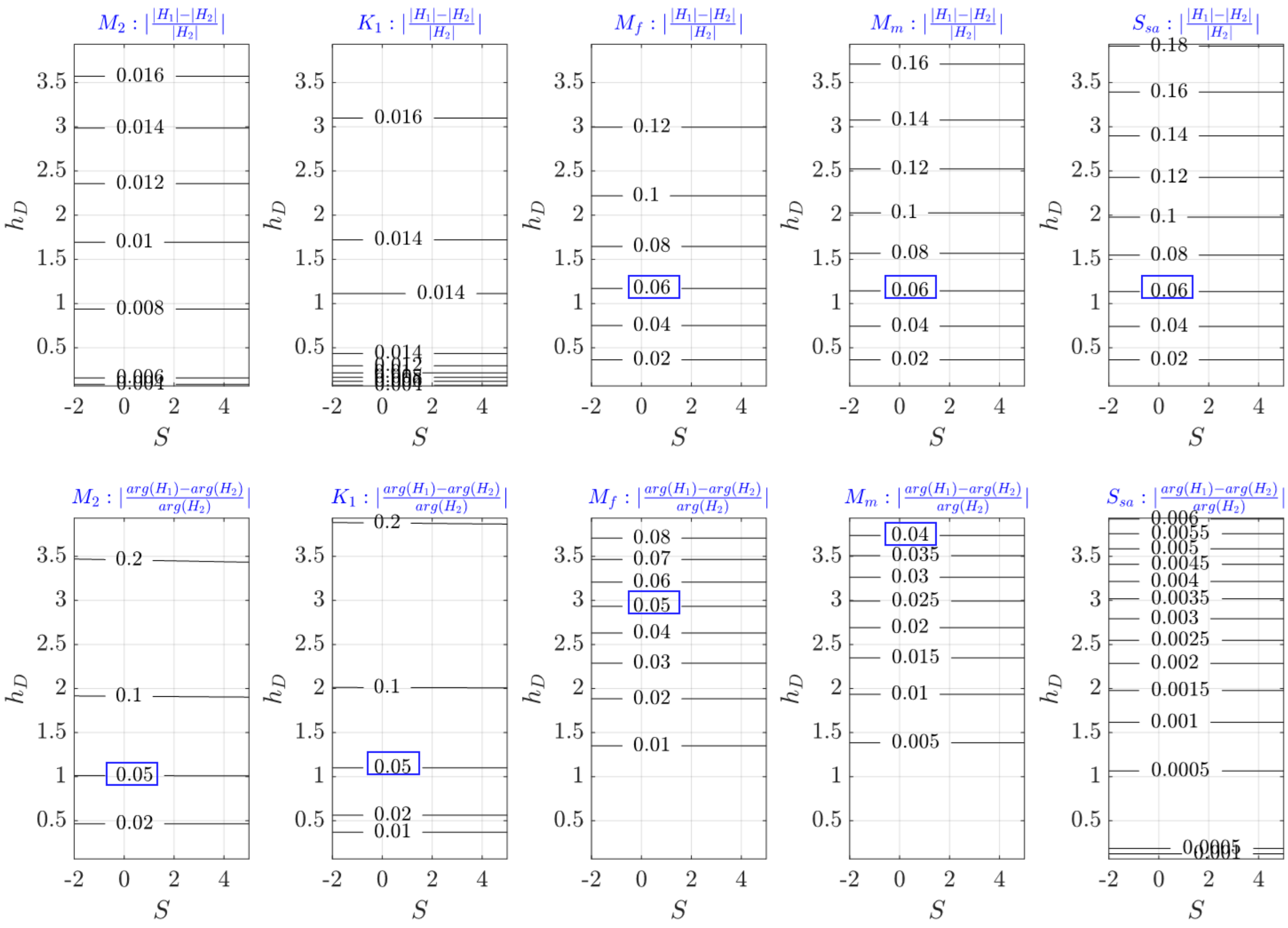

Figure 7: The variation in relative errors between the approximate solutions and the new solutions with the skin effect (S), the frequencies of tidal force, and the nondimensional thickness of aquifer (h_D) for a horizontal well.

4.4 The physical significance of the nondimensional number: $h_D\sqrt{H_D}$

Previously, the nondimensional number, either represented as $h_D\sqrt{H_D}$ or $\sqrt{\frac{hk'}{b'k}}$, was derived mathematically, where h and b' denote the thickness of the aquifer and overlaying layer, respectively, and k and k' symbolize their respective permeabilities. This nondimensional number forms the basis for a quantitative criterion to assess the applicability of the existing solutions derived from the approximate theory that is currently in use. The physical significance of this nondimensional number can be understood by looking at the fluid flows from the overlaying layer to the target aquifer, as shown in Figure 8(a). The fluid flow experiences two resistances: one for diffusion within the overlaying layer (proportional to its thickness b' and inversely proportional to its permeability k'), and the other for diffusion within the target aquifer (also proportional to its thickness h and inversely proportional to its permeability k). The nondimensional number $\sqrt{\frac{hk'}{b'k}}$ can be interpreted as the ratio between the flow resistances of the target aquifer and the overlaying layer. If the flow resistance within the overlaying layer is much greater than that within the target aquifer, the nondimensional number will be less than a specific value of 0.245, which has been derived mathematically in the previous sections. In systems where the nondimensional number less than 0.245, it may be presumed that fluid flows into the target aquifer have time to uniformly distribute and thus have uniform pressure along the vertical direction, consequently, the leakage at the boundary can be approximated as a volumetric source term. Conversely, for systems with the nondimensional number exceeding 0.245, which means the flow resistance within the overlaying layer is not significantly greater or may even be less than that within the target aquifer, pressure gradients within the target aquifer become important and the interior of the target aquifer cannot be assumed to have uniform pressure along the vertical direction, rendering the approximate theory invalid.

From another perspective, the nondimensional number $\sqrt{\frac{hk'}{b'k}}$ can be understood as a descriptor for a physical system's ability to maintain uniform distribution against boundary effects, akin to the role of the Biot number in heat transfer, as illustrated in Figure 8(b). In this figure, the symbols h and δ represent the characteristic length of the object and the thickness of thermal boundary layer, respectively, and K and K' symbolize their respective thermal conductivities. The Biot number is defined as $\mathrm{Bi} = \frac{h_c}{K}h$, signifying the ratio of the conductive heat resistance within the object to the convective heat transfer resistance across the object's boundary. Here, h_c is the convective heat transfer coefficient, K is the thermal conductivity of the object, and h is a characteristic length of the object. After modeling the heat conduction within the thermal boundary layer, the convective heat transfer coefficient can be expressed as $h_c = \frac{K'}{\delta}$, allowing the Biot number to be expressed as $\mathrm{Bi} = \frac{h}{K}\frac{K'}{\delta}$, which takes exactly the same form with the nondimensional number $\sqrt{\frac{hk'}{b'k}}$ except for the presence of the square root operator. Consequently, this number $\sqrt{\frac{hk'}{h'k}}$ can be named as the "hydraulic Biot number" to emphasize its application in hydrology and to set it apart from the original Biot number, which pertains to the field of heat transfer.

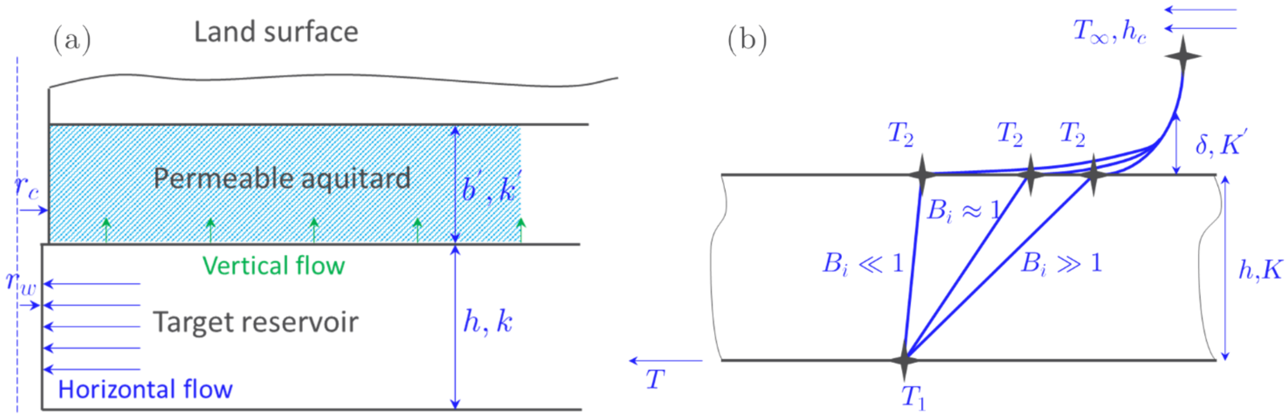

Figure 8: (a) the fluid flows from the overlaying layer to the target aquifer; (b) heat transfer from the surface to the object.

5. Examine the assumption: uniform flow rate along the wellbore

In the previous section, it was concluded that the existing approximate solution exhibits acceptable error and proves suitable only when the nondimensional number $\sqrt{\frac{hk'}{h'k}}$ is less than 0.245. Our new solution extends this upper limitation by solving the standard diffusion equation with appropriate initial and boundary conditions, expressing the leakage as a boundary condition. However, both the approximate and new solutions are solved under the assumption of a uniform flow rate along the wellbore. This assumption can be acceptable for a horizontal well because the horizontal well is parallel to the leakage boundary while this assumption may not always be valid for a vertical well, especially when the thickness of target aquifer is large and the permeability of the overlaying layer is not low. Therefore, it becomes necessary to quantify when this assumption fails and the scope of application for the new solution.

5.1 Two candidates: $\boldsymbol{h_D\sqrt{H_D}}$ and $\boldsymbol{k'/k}$

To quantify when the assumption of uniform flow rate fails, the initial step is to identify a nondimensional number that can reflect the distribution of flow rate along the wellbore. Two potential candidates were considered here. One is $h_D\sqrt{H_D}$ ($\sqrt{\frac{hk'}{h'k}}$), the "hydraulic Biot number" derived earlier. The other is k'/k, the ratio of the permeability of the overlaying layer to that of the target aquifer.

Numerical experiments were then performed to pinpoint the appropriate nondimensional number. Because the distribution of flow rate cannot be obtained directly from the new solution due to the underlying assumption of uniform flow rate during the model's construction, the research methodology shifted to that under the premise of assuming a uniform distribution of flow rate, the focus is on investigating the pressure distribution along the wellbore. If the variation in pressure distribution remains within 10%, the assumption of uniform flow rate distribution is considered correct; otherwise, it is deemed incorrect.

Subsequently, the effects of varying $h_D\sqrt{H_D}$ and k'/k on wellbore pressure distribution are explored under two extreme scenarios for a vertical well: $\frac{h_D}{b_D} = 0.048$ (very thin target aquifer relative to the overlaying layer) and $\frac{h_D}{b_D} = 6$ (very thick target aquifer relative to the overlaying layer). The results are presented in Figure 9. In this figure, the x-axes represent amplitude and phase of the transfer function between wellbore pressure and Earth tides. Because the referenced Earth tides are consistent, the amplitude and phase of the transfer function can serve as representations of the relative amplitude and phase of the wellbore pressure. The y-axis indicates height from the well bottom. Each curve corresponds to specific values of $h_D\sqrt{H_D}$ and k'/k, identifiable by the color in the color bar. From Figure 10, it is observed that the phase of wellbore pressure remains nearly consistent from the well bottom to wellhead, while the amplitude of wellbore pressure changes along the wellbore. Two representative curves are highlighted: one with $h_D\sqrt{H_D} = 0.245$ and the other is marked with $k'/k = 0.09$ or 0.1. Under both two extreme scenarios, a small "hydraulic Biot number" ($h_D\sqrt{H_D} =$

0.245) consistently maintains a pressure distribution close to uniform along the wellbore, while a small value of k'/k (0.09 or 0.1) fails to ensure uniformity in the thick aquifer scenario. This illustrates that the uniformity of pressure distribution can be controlled by the "hydraulic Biot number" instead of k'/k. Thus, "hydraulic Biot number" is the key nondimensional number that reflects the distribution of flow rate along the wellbore.

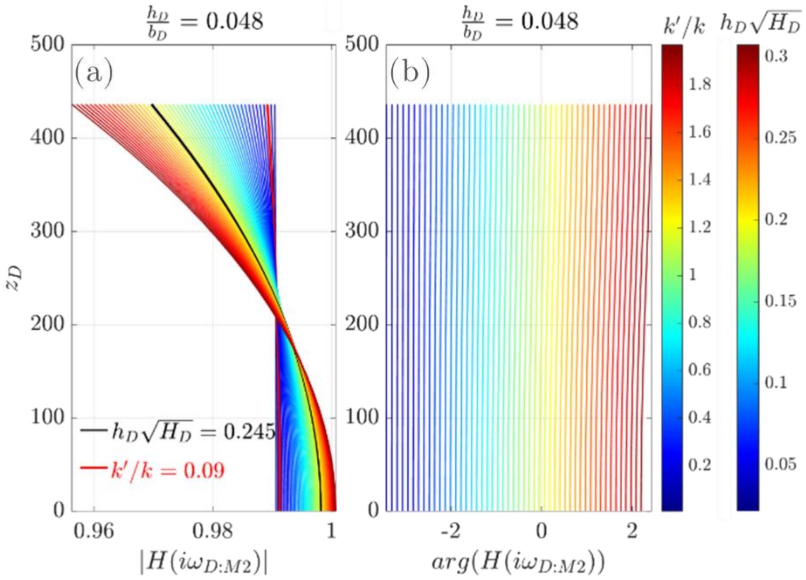

Figure 9: Wellbore pressure distribution under $\frac{h_D}{b_D} = 0.048$: (a) amplitude; (b) phase.

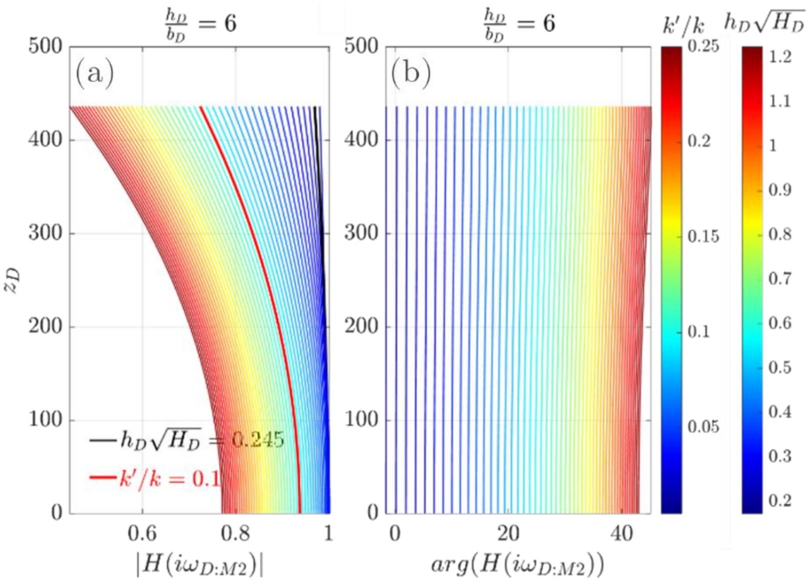

Figure 10: Wellbore pressure distribution under $\frac{h_D}{b_D} = 6$: (a) amplitude; (b) phase.

5.2 The condition for the assumption of uniform flow rate along wellbore

After determining the crucial nondimensional number that reflects the distribution of flow rate along the wellbore, Figure 11 illustrates the amplitude ratios of wellhead pressure to well bottom pressure variation with $h_D\sqrt{H_D}$, under different tidal constituents with varying frequencies (semidiurnal M_2, diurnal K_1 and half month M_f) and different aquifer thickness ranging from $h_D = 1$ to 100.

From earlier discussions, if the variation in pressure distribution remains within 10% (the amplitude ratio of wellhead pressure to well bottom pressure falls in the range of 0.9 to 1.1), the assumption of uniform flow rate distribution is considered correct; otherwise, it is deemed incorrect. Assuming $h^2/k > 10^{13}$, which holds true for most aquifers, two boundaries are determined. The lower boundary, marked with a green curve in Figure 11, is determined when h^2/k is a large value. The upper boundary, marked with a blue curve, is determined by $h^2/k = 10^{13}$. Two critical points, labeled A and B, are determined by the intersections of the lines y=0.9 and y=1.1 with the two boundaries. The minimum $h_D\sqrt{H_D}$ values of points A and B establish the upper limit where the assumption of uniform flow rate distribution remains valid. With an increase in the tidal period (from M_2 to M_f), the value of $h_D\sqrt{H_D}$ corresponding to point A remains constant at 0.475, while that corresponding to point B decreases from around 0.8 to 0.3. This behavior occurs because the aquifer tends to be more confined under tidal force with high frequency and tends to be more open under tidal force with low frequency (Wang, 2000). A more open aquifer leads to a tighter upper limit where the assumption of uniform flow rate distribution is valid. Because the amplitude of tidal constituent M_f is too small, semidiurnal and diurnal tidal constituents are primarily analyzed to characterize the aquifer. Thus, by comparing the $h_D\sqrt{H_D}$ values of lower and upper boundaries for semidiurnal and diurnal tidal constituents, the upper limit for the assumption of uniform flow rate distribution is identified as $h_D\sqrt{H_D} = 0.475$.

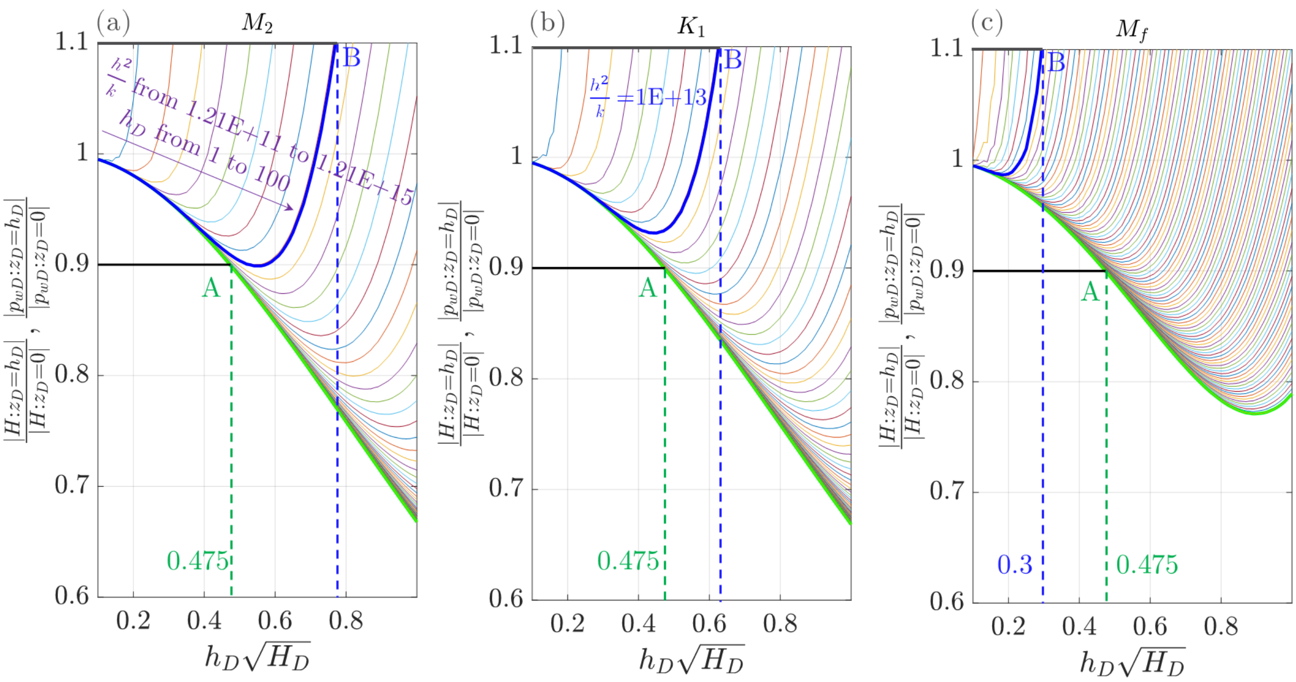

Figure 11: The amplitude ratios of wellhead pressure to well bottom pressure variation with $h_D\sqrt{H_D}$: (a) semidiurnal constituent; (b) diurnal constituent; (c) half-month constituent.

In summary, the quantitative conditions for the application of both the approximate solution and the new solution are detailed in Table 4. For a vertical or horizontal well in a semiconfined aquifer, the approximate solution works only when $h_D\sqrt{H_D} < 0.245$. Meanwhile, the new solution is valid when $h_D\sqrt{H_D} < 0.475$ for a vertical well and is always valid for a horizontal well. It is noted that when $h_D\sqrt{H_D} \geq 0.475$, there is no existing analytical solution that works for a vertical well.

Table 4: The quantitative conditions for the application of both the approximate solution and the new solution

	$h_D\sqrt{H_D} < 0.245$	$0.245 \leq h_D\sqrt{H_D} < 0.475$	$h_D\sqrt{H_D} \geq 0.475$
Vertical wells	Approximate solution/ New solution	New solution	No existing solution
Horizontal wells	Approximate solution/ New solution	New solution	New solution

6. Application of the new leaky aquifer model to the Arbuckle Aquifer, Oklahoma

The new solution was applied to the Arbuckle aquifer to illustrate its enhanced validity compared to the existing one. Wang et al. (2018) developed the current semiconfined model and applied it to assess the vertical leakage of the Arbuckle aquifer. The data analyzed in their study was collected from a deep monitoring well in the Arbuckle aquifer in Oklahoma by the US Geological Survey. Table 5 provides detailed information on both the well and the aquifer parameters to characterize this specific well-aquifer system. According to Wang's findings, there is a 12.5° phase advance between the water level tidal response and the theoretical tide. Given the thickness of the aquitard (277m) and the storativity of the aquifer ranging from 2.6×10^{-6} to 2.7×10^{-5}, the estimated hydraulic conductivity of the aquitard is between 3×10^{-8} to 3×10^{-7} m/s, based on the existing approximate semiconfined model. Consequently, the permeability of the aquitard is estimated to be around 3×10^{-15} to 3×10^{-14} m^2.

Table 5: Details parameters to characterize the Arbuckle aquifer

Parameters	Values	Parameters	Values
Well depth	960m	Well radius	11cm
Casing radius	3.65cm	Thickness of aquitard	277m
Thickness of aquifer	48m	Permeability	2×10^{-14} to 3×10^{-12} m^2
Transmissivity	9.6×10^{-6} to 1.4×10^{-3} m^2/s	Storativity	2.6×10^{-6} to 2.7×10^{-5}

Given the permeabilities and thickness of both the aquifer and aquitard, the "hydraulic Biot number" $h_D\sqrt{H_D}$ can be calculated, as shown in Figure 12(a). In this figure, the white area represents the "hydraulic Biot number" less than 0.245, indicating that both the existing approximate solution and the new solution are applicable within this region. However, in the blue area where the "hydraulic Biot number" exceeds 0.245, the new solution should be analyzed in preference to the existing approximation, although this blue area represents a relatively small region.

A value of $h_D\sqrt{H_D}$ is selected from the blue area, marked with a red star. With given values for the aquifer's permeability and the estimated aquitard's permeability, this value of $h_D\sqrt{H_D}$ is around 0.4. Both the existing and the new solutions are applied to this specific case. The corresponding phase advance variations with leakage coefficients are shown in Figure 12(b) and the relative errors of phase advance between the existing and new models are shown in Figure 12(c). In these figures, the red line represents the result of Gao and Wang's model, while the blue line corresponds to the new model. The intersection points between these two lines and the black horizontal line (which represents the phase advance equal to 12.5°) result in two leakage coefficients: 1.1×10^{-6} and 1.2×10^{-6}, corresponding to the existing and new models, respectively. The relative error in phase advance between these two models is around 10% given the estimated leakage coefficient and the relative error in estimated leakage coefficients between these two models is about 9% given the phase advance equal to 12.5°. Although a 10% error is not a major error, these results nonetheless highlight the enhanced validity of the new solution compared to the existing one and expand the applicability of tidal analysis to aquifers with relatively large thickness and leakage.

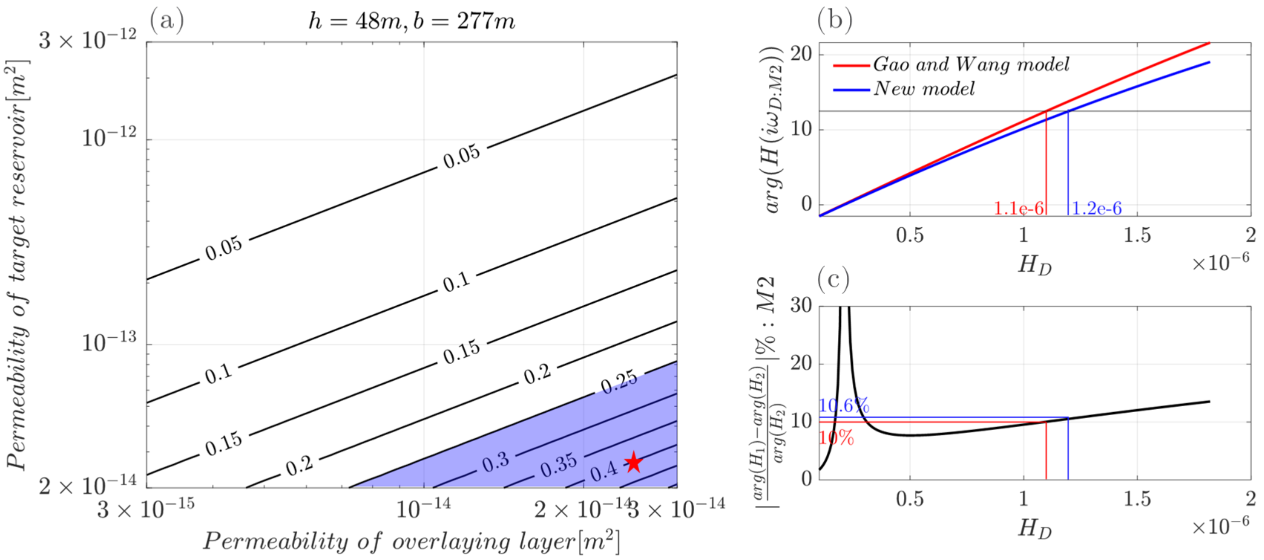

Figure 12: (a) the "hydraulic Biot number" $h_D\sqrt{H_D}$ for the Arbuckle aquifer; (b) phase advance variations with leakage coefficients when $h_D\sqrt{H_D} = 0.41$; (c) relative errors of phase advance between the existing and new models when $h_D\sqrt{H_D} = 0.41$.

7. Summary and Conclusions

Our work can be summarized as follows:

1. Accurate solutions for tidal behaviors of a vertical well and a horizontal well in aquifers with relatively large thickness and leakage were obtained by solving the standard diffusion equation with appropriate initial and boundary conditions, expressing the leakage as a boundary condition instead of treating it as a volumetric source term in the diffusion equation. The difference between this solution and that of Hantush (1967) is that Hantush analyzed the pump test results and did not take the tidal force into consideration.
2. The "hydraulic Biot number" was derived mathematically, dependent on the thickness of the aquifer and overlying layer, as well as their respective permeabilities and expressed as $h_D\sqrt{H_D}$. This nondimensional number "hydraulic Biot number" forms the basis for a quantitative criterion to assess the applicability of the existing approximate solution. The physical significance of this number was discussed and it can be understood as a descriptor for a physical system's ability to maintain uniform distribution against boundary effects, akin to the role of the Biot number in heat transfer.
3. Two key assumptions used in the existing approximate solution are assessed: one is relative thin aquifer and relative low permeability of aquitard and the other is uniform flow rate along wellbore. The quantitative criterion of the applicability of both the existing solution and the new solution were concluded. In the case of a vertical well, the existing solution exhibits acceptable error and proves suitable only the nondimensional number is less than 0.245. Our new solution extends this upper limitation to 0.475. However, when the number is greater than 0.475, both the existing solution and our new solution are invalid due to the invalid uniform flow rate assumption. For a horizontal well, when the number is less than 0.245, the existing solution is suitable with acceptable error. Our new solution effectively overcomes this limitation.
4. The new solution and existing solution were applied to the case of the Arbuckle aquifer to demonstrate the improved validity of the new solution compared to the existing one.

Acknowledgements

This research was supported by the Stanford University Industrial Affiliates Program on Innovation in Energy Systems Monitoring and Testing (SUETRI-D). We would like to thank the anonymous reviewers for contributing their time and expertise to review and enhance the original manuscript. The paper is theoretical, and data were not used, nor created for this research.

References

Agnew, D. C. (2012). SPOTL: Some programs for ocean-tide loading. Technical Report, Scripps Institution of Oceanography.

Allègre, V., Brodsky, E. E., Xue, L., Nale, S. M., Parker, B. L., & Cherry, J. A. (2016). Using earth-tide induced water pressure changes to measure in situ permeability: A comparison with long-term pumping tests. Water Resources Research, 52(4), 3113-3126. http://doi.org/10.1002/2015WR017346

Arditty, P. C., Ramey Jr, H. J., Nur, A. M.(1978). Response of a closed well reservoir system to stress induced by earth tides. Paper Number: SPE-7484-MS, SPE Annual Fall Technical Conference and Exhibition. Society of Petroleum Engineers. http://doi.org/10.2118/7484-MS

Bredehoeft, J. D. (1967). Response of well-aquifer systems to earth tides. Journal of Geophysical Research, 72(12), 3075–3087. http://doi.org/10.1029/JZ072i012p03075

Burbey, T. J. (2010). Fracture characterization using Earth tide analysis. Journal of Hydrology, 380(3-4), 237-246. https://doi.org/10.1016/j.jhydrol.2009.10.037

Burbey, T. J., Hisz, D., Murdoch, L. C., & Zhang, M. (2012). Quantifying fractured crystalline-rock properties using well tests, earth tides and barometric effects. Journal of Hydrology, 414, 317-328. https://doi.org/10.1016/j.jhydrol.2011.11.013

Cutillo, P. A., & Bredehoeft, J. D. (2011). Estimating aquifer properties from the water level response to earth tides. Groundwater, 49(4), 600-610. https://doi.org/10.1111/j.1745-6584.2010.00778.x

Dean, G., Hardy, R., and Eltvik, P. (1994). Monitoring compaction and compressibility changes in offshore chalk reservoirs. SPE Formation Evaluation, 9(01):73–76. http://doi.org/10.2118/23142-PA

Doan, M. L., Brodsky, E. E., Prioul, R., & Signer, C. (2006). Tidal analysis of borehole pressure-A tutorial. University of California, Santa Cruz, 25, 27.

Gao, X., Sato, K., & Horne, R. N. (2020). General solution for tidal behavior in confined and semiconfined aquifers considering skin and wellbore storage effects. Water Resources Research, 56(6), e2020WR027195. http://doi.org/10.1029/2020WR027195

Gieske, A., & De Vries, J. J. (1985). An analysis of earth-tide-induced groundwater flow in eastern Botswana. Journal of Hydrology, 82(3-4), 211–232. http://doi.org/10.1016/0022-1694(85)90018-6

Hantush, M. S. (1960). Modification of the theory of leaky aquifers. Journal of Geophysical Research, 65(11), 3713-3725. http://doi.org/10.1029/JZ065i011p03713

Hantush, M. S. (1967). Flow of groundwater in relatively thick leaky aquifers. Water Resources Research, 3(2), 583-590. http://doi.org/10.1029/WR003i002p00583

Horne, R. N. (1995). Modern well test analysis. Petroway, Inc.

Hsieh, P. A., Bredehoeft, J. D., & Farr, J. M. (1987). Determination of aquifer transmissivity from Earth tide analysis. Water resources research, 23(10), 1824-1832. http://doi.org/10.1029/WR023i010p01824

Jacob, C. E. (1939). Fluctuations in artesian pressure produced by passing railroad-trains as shown in a well on Long Island, New York. Eos, Transactions American Geophysical Union, 20(4), 666-674. http://doi.org/10.1029/TR020i004p00666

Lai, G., Ge, H., Xue, L., Brodsky, E. E., Huang, F., & Wang, W. (2014). Tidal response variation and recovery following the Wenchuan earthquake from water level data of multiple wells in the nearfield. Tectonophysics, 619, 115-122. https://doi.org/10.1016/j.tecto.2013.08.039

Liang, X., Wang, C. Y., Ma, E., & Zhang, Y. K. (2022). Effects of unsaturated flow on hydraulic head response to Earth tides–An analytical model. Water Resources Research, 58(2), e2021WR030337. https://doi.org/10.1029/2021WR030337

Lu, X., Sato, K., & Horne, R. N. (2022, September). Analysis of Tidal Behavior of a Horizontal Well to Determine Reservoir Properties. Paper SPE-210166-MS presented at the SPE Annual Technical Conference and Exhibition, October 3–5, 2022. http://doi.org/10.2118/210166-MS

Matsumoto, K., Sato, T., Takanezawa, T., & Ooe, M. (2001). GOTIC2: A program for computation of oceanic tidal loading effect. Journal of the Geodetic Society of Japan, 47(1), 243-248.

McMillan, T. C., Rau, G. C., Timms, W. A., & Andersen, M. S. (2019). Utilizing the impact of Earth and atmospheric tides on groundwater systems: A review reveals the future potential. Reviews of Geophysics, 57(2), 281-315. http://doi.org/10.1029/2018RG000630

Melchior, P. (1966). The tides of the planet earth. Pergamon Press, Oxford.

Merritt, M. L. (2004). Estimating hydraulic properties of the Floridan aquifer system by analysis of earth-tide, ocean-tide, and barometric effects, Collier and Hendry Counties, Florida. Reston, VA: US Department of the Interior, US Geological Survey.

Rau, G. C., McMillan, T. C., Andersen, M. S., & Timms, W. A. (2022). In situ estimation of subsurface hydro-geomechanical properties using the groundwater response to semi-diurnal Earth and atmospheric tides. Hydrology and Earth System Sciences, 26(16), 4301-4321. http://doi.org/10.5194/hess-26-4301-2022

Robinson, E. S., & Bell, R. T. (1971). Tides in confined well-aquifer systems. Journal of Geophysical Research, 76(8), 1857–1869. http://doi.org/10.1029/JB076i008p01857

Rojstaczer, S., & Agnew, D. C. (1989). The influence of formation material properties on the response of water levels in wells to Earth tides and atmospheric loading. Journal of Geophysical Research: Solid Earth, 94(B9), 12403-12411. https://doi.org/10.1029/JB094iB09p12403

Sato, K. (2006). Monitoring the underground migration of sequestered carbon dioxide using Earth tides. Energy conversion and management, 47(15-16), 2414-2423. http://doi.org/10.1016/j.enconman.2005.11.005

Sato, K., & Horne, R. N. (2018). Time-lapse analysis of pressure transients due to ocean tides for estimating CO2 saturation changes. International Journal of Greenhouse Gas Control, 78, 160-167. http://doi.org/10.1016/j.ijggc.2018.08.005

Sato, K., Tamura, Y., Osato, K., & Horne, R. N. (2022). Assessing poroelastic properties of a geothermal reservoir by tidal signal analysis. Geothermics, 100, 102352. http://doi.org/10.1016/j.geothermics.2022.102352

Simon, J. B., Fulton, P. M., & Xue, L. (2021). Hydrogeologic property estimation in plate boundary observatory boreholes using tidal response analysis. Geofluids, 2021, 1-19. https://doi.org/10.1155/2021/6697021

Skempton, A. W. (1954). The pore-pressure coefficients A and B. Geotechnique, 4(4), 143-147. http://doi.org/10.1680/geot.1954.4.4.143

Thambynayagam, R. K. (2011). The diffusion handbook: applied solutions for engineers. New York: McGraw-Hill Professional.

Valois, R., Rau, G. C., Vouillamoz, J. M., & Derode, B. (2022). Estimating hydraulic properties of the shallow subsurface using the groundwater response to Earth and atmospheric tides: A comparison with pumping tests. Water Resources Research, 58(5), e2021WR031666.

http://doi.org/10.1029/2021WR031666

Van der Kamp, G., & Gale, J. E. (1983). Theory of earth tide and barometric effects in porous formations with compressible grains. Water Resources Research, 19(2), 538-544. http://doi.org/10.1029/WR019i002p00538

Wang, C. Y., Doan, M. L., Xue, L., & Barbour, A. J. (2018). Tidal response of groundwater in a leaky aquifer—Application to Oklahoma. Water Resources Research, 54(10), 8019-8033. http://doi.org/10.1029/2018WR022793

Wang, H. F. (1993). Quasi-static poroelastic parameters in rock and their geophysical applications. Pure and Applied Geophysics, 141, 269-286. http://doi.org/10.1007/BF00998332

Wang, H. F. (2000). Theory of linear poroelasticity with applications to geomechanics and hydrogeology (Vol. 2). Princeton University Press. http://doi.org/10.1515/9781400885688

Xue, L., Li, H. B., Brodsky, E. E., Xu, Z. Q., Kano, Y., Wang, H., Mori, J. J., Si, J. L., Pei, J. L., Zhang, W., Yang, G., Sun, Z. M., and Huang, Y. (2013). Continuous permeability measurements record healing inside the Wenchuan earthquake fault zone. Science, 340(6140):1555–1559. https://doi.org/10.1126/science.1237237

Zhang, Y., Wang, C. Y., Fu, L. Y., & Yang, Q. Y. (2021). Are deep aquifers really confined? Insights from deep groundwater tidal responses in the North China Platform. Water Resources Research, 57(11), e2021WR030195. https://doi.org/10.1029/2021WR030195

Zhu, A. Y., & Wang, C. Y. (2020). Response of leaky aquifers to Earth tides–Interpreted with numerical simulation. Journal of Hydrology, 581, 124458. https://doi.org/10.1016/j.jhydrol.2019.124458